4 The Second Energy Transfer Process: Plasma–Particle Interactions

4.1 Injection of Powders

There are several ways to inject powder particles into the plasma jet. Figure 4-1 shows injection perpendicular to the jet at the point of exit of the jet from the anode nozzle (position 1), 'upstream' or 'downstream' injection at an angle to the jet axis (position 2), or injection directly into the nozzle (position 3). Upstream injection is used when increased residence time of the particles in the jet is required, for example to melt high refractory materials with high melting points. Downstream injection protects the powder material from excessive vaporization. Experiments with molybdenum and alumina coatings showed that the cohesion of coatings and their tensile strengths increase with oblique injection [1].

Also, experiments have been conducted with coaxial powder injection where the powder enters through a bore in the cathode, and is swept along the total length of the plasma jet for maximum residence time (position 4). This configuration, however, tends to disturb the smooth plasma flow and thus creates turbulences and eddies that may damage the nozzle walls. Problems may also occur with clogging the plasma paths with excess powder. A somewhat different approach has been taken by Maruo *et al.* [2] by feeding powder axially into the space between three thoriated tungsten cathodes set at 120° around the plasmatron axis. As three individual anode spots are formed the thermal and erosion-damage of the anode nozzle was diminished.

4.2 Feed Materials Characteristics

Feed materials can be used in form of solid wires, rods, filled wires and powders (Table 4-1). One of the main materials requirement is that melting must occur without decomposition or sublimation.
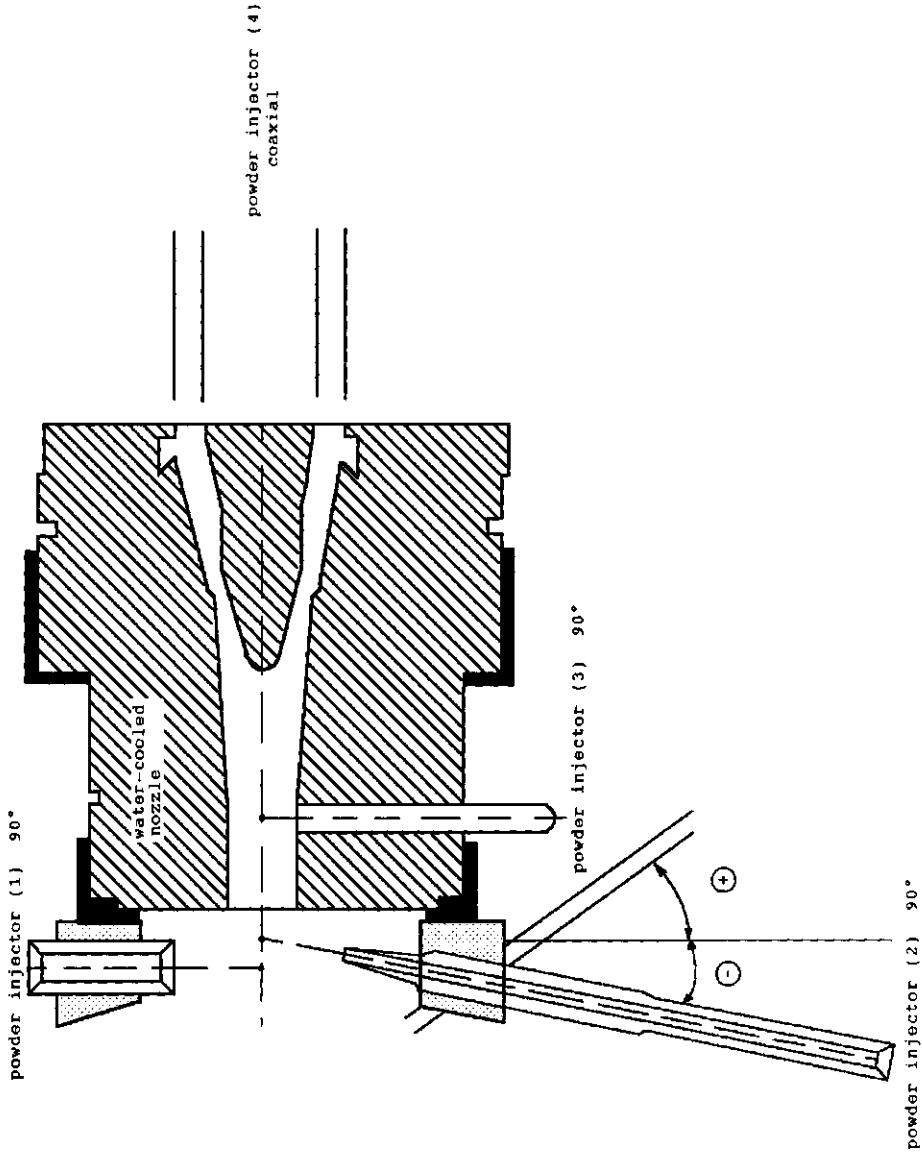
Figure 4-1. Powder injection options (see text).

Table 4-1. Spray coating materials and their standards (after reference [3]).

Parameter	Solid wires	Solid wires	Rods	Filled plastic tubes	Filled wires	Powders
German standard DIN	8566 Part 1	8566 Part 2	8566 Part 3	8566 Part 3	–	32529 65097
Spraying process	flame spraying	electric arc spraying	flame spraying	flame spraying	electric arc spraying	flame and high-energy spraying
Diameter, mm	1.5–4.16	1.6–3.2	3.15, 4.75, 6.3	1.5–6.3	2 and 3.2	5–180[a]
Length, mm		450 and 600				
Main materials	steels, nonferrous metals and alloys, molybdenum		oxides	metals, oxides	Fe–Cr–C carbides	complete range

[a] Particle size, μm

4.2.1 Solid Wires, Rods and Filled Wires

Solid wires and rods as well as filled wires are mostly used in flame and electric arc spraying operations. Steel and nonferrous metals and alloys can be shaped into wires. A special technique (Bifilar system, OSU Oberflächentechnik KG, Bochum, Germany) allows the simultaneous spraying of two wires of different compositions to form a pseudo-alloy coating [3]. Rods of metal oxide compositions are being manufactured by the Rokide process by Norton Industrial Ceramics, Worcester, MA, USA. Filled wires are composed of hollow steel or nickel tubes filled with powder of tungsten, chromium carbide or compositions of the Fe–B system [4]. Also, an outer tube of polymeric material filled with metal oxide or metal powder can be used (Sfecord, Société de fabrication d'elements catalytiques, France).

4.2.2 Powders

Powder particle diameters are generally between 5 and 200 μm with a preferred range of 20–100 μm, and a median diameter of 50 μm for APS applications. Many materials can be made into powders by a variety of techniques to yield spray powders with a narrow grain size distribution, good flowability and optimum deposition efficiency for optimized spray parameter ranges. Powders utilized for flame spraying must have melting points not exceeding 2 500 K because of the rather low temperatures in the flame. Special conditions apply for HVOF and detonation gun techniques. Powders designed for plasma spraying operations must be able to withstand the high mechanical and thermal stresses excerted on them by the hot, high speed plasma jet. Thus powders manufactured by agglomeration of finer particles must be thoroughly sintered to guarantee mechanical stability. Very fine reactive plasma spray powders with an extremely narrow grain size distribution range for vacuum spraying (LPPS) operations demand the highest quality specifications and thus very strict quality control procedures.

To produce spray powders, precursor materials must be melted or sintered with subsequent size reduction by crushing, grinding and attrition milling. Mixing of powders and classification are also important process steps. Specialized powders for a variety of industrial applications are being produced by spray drying, fluidized bed sintering, agglomeration, fusing/melting, plasma spheroidizing, atomizing, surface coatings and sol–gel processes. Figure 4-2 shows schematically different powder types, particle shapes and microstructures. Figure 4-3 relates the particle porosity to the structural fineness, i.e. the crystal size. Electronmicrographs shown in Figure 4-4 demonstrate the wide variability of thermal spray powders ranging from gas- and water-atomized (a,b) to fused and crushed (c), clad (d), sintered (e) or agglomerated (f) powders [5].

For nonstandard applications special powders must be designed and thoroughly characterized in terms of chemical composition, microstructure, physical properties, morphology and spraying behavior by a large spectrum of methods. Development of new spray powders is an extremely involved task that has to be controlled at all process stages by established methods of total quality management (TQM) including

Powder Type Manufacture	fused milled	sintered milled	agglomerated (sintered)	spheroidized	atomized
Particle Shape	blocky-angular	blocky-angular	spherical	spherical	spherical-irregular
Microstructure					
-Porosity	dense	dense-porous	porous	dense-hollow	porous-hollow
-Crystal size	coarse-fine	coarse-fine	medium-fine	medium-fine	fine
-Homogeniety	alloyed	alloyed	alloyed (heterogeneous)	alloyed (heterogeneous)	alloyed

Production Specific Powder Characteristics / Powder Types

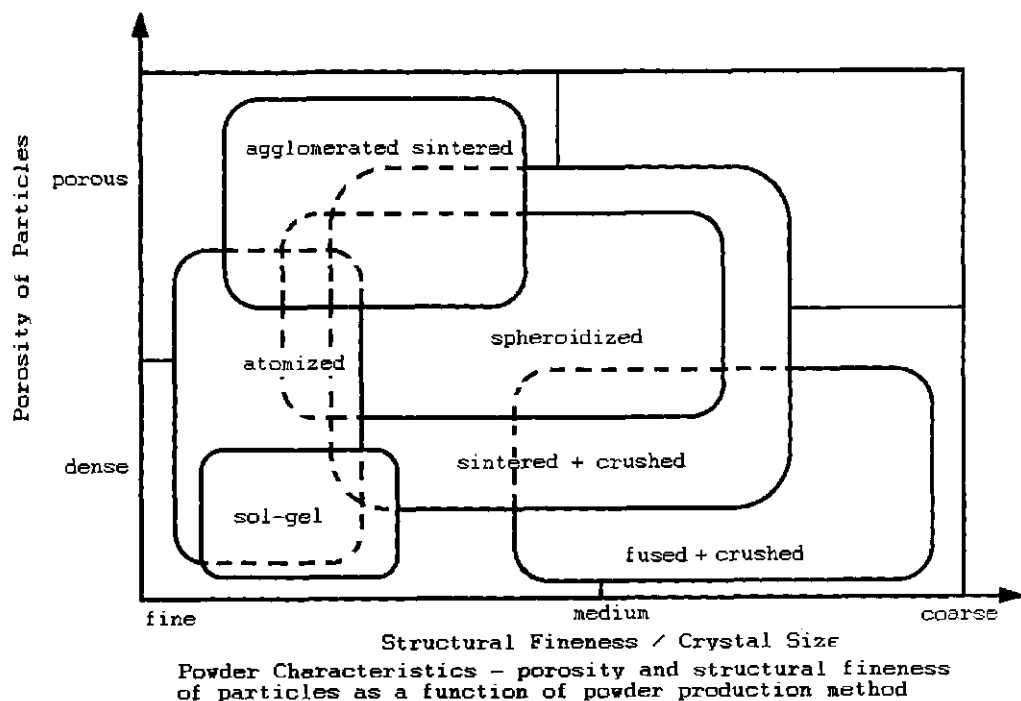**Figure 4-2.** Different powder types, particle shapes, and microstructures.

Figure 4-3. Relation of porosity and crystal size of powder particles as a function of the production method.
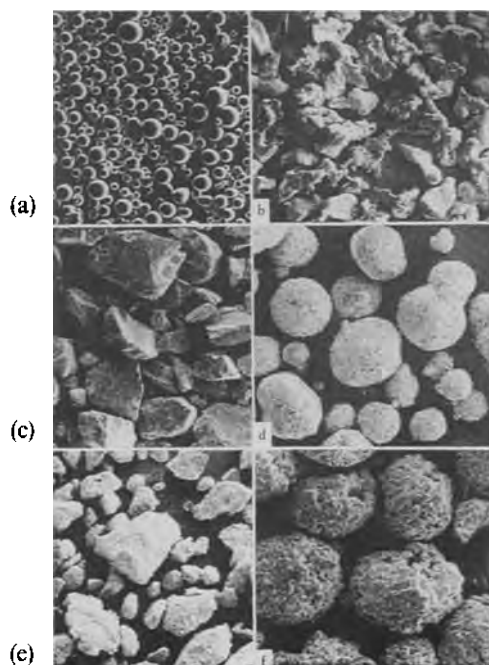

(a)

(c)

(e)

Figure 4-4. Powder morphology dependent on the production method: gas- and water-atomized (a,b), fused and crushed (c), clad (d), sintered (e) and agglomerated (f) powders [5].

SDE, SPC and QFD. Important morphological parameters are shape, surface properties, porosity, homogeneity and phase composition [6]. Figure 4-5 shows a compilation of testing procedures and quality control measures for plasma spray powders and coatings [3]. For more details on methods of powder production and characterization see [7].

The size of the particles is of critical importance. The size distribution is usually statistical, i.e. follows a Gaussian or log-normal distribution. While the median size for an average powder used in plasma spraying is around 40 µm, there are much smaller and much larger particles available. The small particles will evaporate rather quickly prior to impact at the surface, whereas the larger ones melt only incompletely, and may actually rebound from the surface or fall out of the jet owing to gravitational forces. In either case these small and large particles are lost from the flame or plasma jet and thus reduce the deposition efficiency. This deposition efficiency is defined as the ratio between the number of particles deposited at the surface to the number of particles sprayed. Evidently a high deposition efficiency is of overriding economical importance so that its optimization constitutes a crucial step in any coating development operation.

4.2.2.1 Atomization

This technique is frequently used to produce powders based on iron-, cobalt-, nickel- and aluminum alloys. The particles exhibit a distinct difference in shape depending on the method of quenching. Gas-atomized particles (Fig. 4-4a, Fig. 4-6a) are highly spherical whereas water-atomized particles (Fig. 4-4b) have a more angular shape. As a consequence, different coating characteristics are obtained when these two powder types are thermally sprayed at identical feed rates and plasma parameters even if comparable particle-size distributions are used. This also means that the parameters optimized for gas-atomized powder can not be uncritically transferred to water-atomized powders. In this case, clogging of the spray nozzle, discoloration, and/or cracking and spalling of the coating can result. On the other hand, spraying gas-atomized powders with parameters optimized for water-atomized powder will generally result in low deposition efficiency, increased coating porosity, and poor adhesion.

4.2.2.2 Fusion and Crushing

This technique of manufacturing is applied to ceramics and cermet (carbide) powders (Fig. 4-6b) as well as to brittle metals. Adjusting the solidification rate during fusion (casting) yields differences in the crystallinity. Subsequent crushing results in a wide range of particle shapes and consequently in apparent particle density. These variations in processing parameters lead to a variability in coating density, macrohardness and wear resistance, and also thermal-cycling fatigue of oxide thermal barrier coatings. Special techniques to manufacture yttria-stabilized zirconia powders for thermal barrier coatings include the arc-fuse/crush, hollow-spherical-powder (HOSP)/ plasma-fuse, and arc-fuse/spray-dry processes [5]. In particular, *arc-fuse/crush powders* (Fig. 4-4c) are being produced by fusing, crushing and screening a premixed
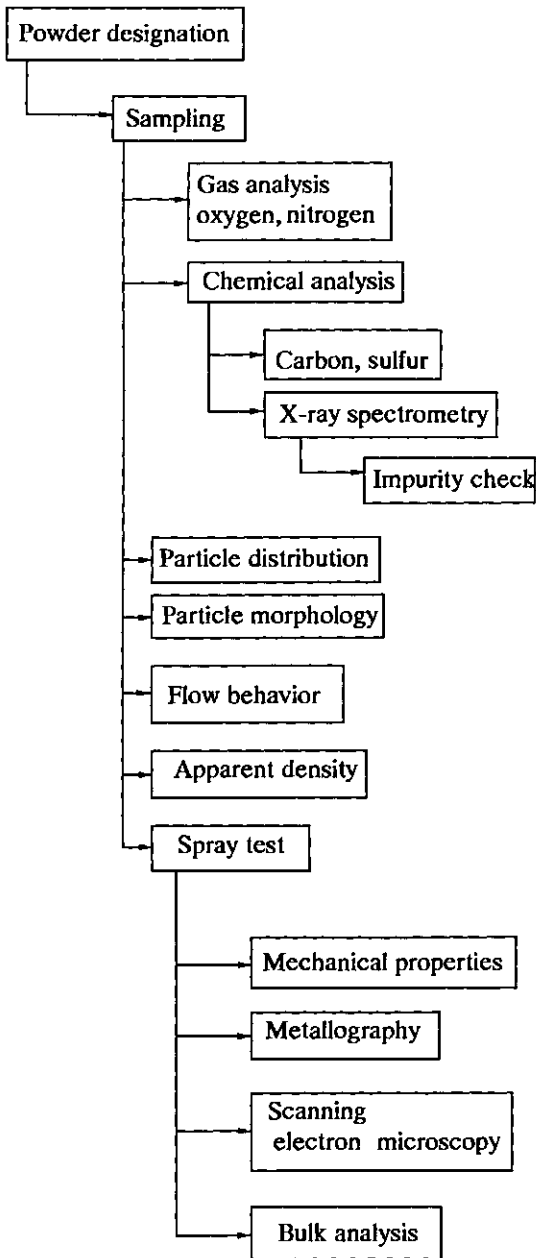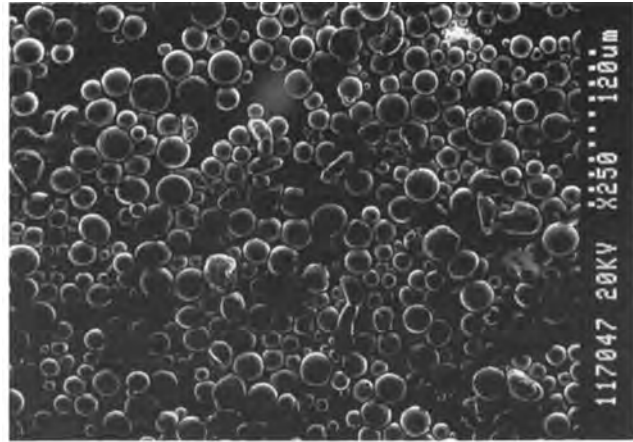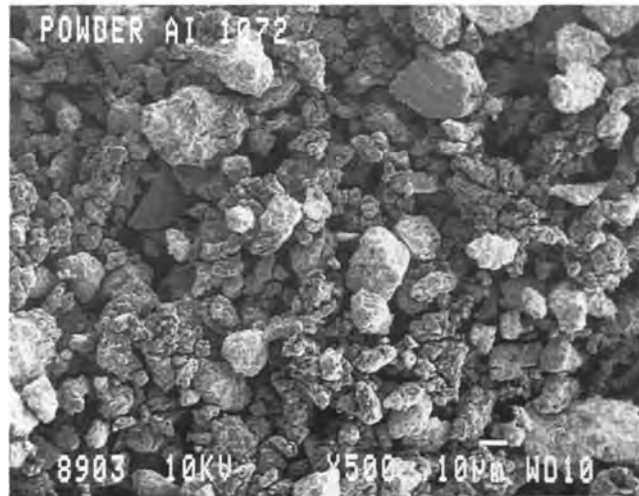
Figure 4-5. Testing procedures and quality control for plasma spray powders and coatings [3].

Figure 4-6. Water-atomized 85Fe15Si (a) and arc-fused/crushed 88WC12Co (b) powder particles [8].

(a)

(b)

powder of 7–8 mol % yttrium oxide and zirconia. The particles obtained are irregularly shaped and have a rather broad size distribution. Thus they flow not too well, and because of their angular shape can be difficult to melt in a non-optimized plasmatron configuration.

HOSP powders are produced by premixing, spray drying, fusing the product in a plasma jet, and screening. The hollow spherical particles thus produced show excellent flowability, and their low mass guarantees easy melting. However, the thin-shelled particles can be destroyed in the plasma jet by the large forces excerted on them. *Arc-fuse/spray-dry powders* combine micronizing and spray-drying with the arc-fuse/crush process. Even though the particles are often hollow their walls are porous in contrast to the walls of the HOSP powders. This results in a tenfold increase in surface area. Such powders are advantageous if very high coating porosities

are required as needed in effective thermal barrier and bioceramic coatings (see Secs. 6.2, 6.3).

4.2.2.3 Compositing

Combining two or more dissimilar materials is achieved by chemical cladding (Fig. 4-4d), organic bonding and/or sintering. Typically Ni–Al composite powders are produced by this method. Spatial variation of the ratios of the materials in the cladding, or loss of material due to preferential vaporization/evaporation may result in nonuniform chemical composition, hardness and fracture toughness of the coating. Clad-powder coatings frequently have exceptionally high adhesion strengths surpassing those of coatings produced from gas- or water-atomized powders.

Composite powders are the first stage of composite materials. At the Institute of Materials Science, Rheinisch-Westfälische Technische Hochschule (RWTH) Aachen, Germany, ceramics, metals and polymers can be combined into micropellets with one or more reinforcing material (fibers, particles) by spray drying [9]. The starting powders are distributed homogeneously in the micropellets that show an excellent flowability. Also, a special technique for coating powders of any morphology and from submicron up to several hundred micrometer size was developed using the so-called HYPREPOC (HYdrogen Pressure-REducing POwder Coating) process. An inorganic or organic metal salt (sulfates, nitrates, acetates, carbonates, chlorides etc.) solution is reduced in an autoclave by hydrogen in the presence of a powder of the core material. The coatings so produced are smooth, dense and highly adherent to the core particles. Successive precipitation steps result in either very thick coatings or multilayer coatings of dissimilar materials. The advantage of the HYPREPOC process is that nearly any material can be used either as core material or as a coating. Core material can be coated regardless whether the particles are angular or spherical.

4.2.2.4 Agglomeration

The agglomeration process is carried out through a sequence of different steps including pelletizing, pressing or spray drying. Variation of the processing parameters leads to large differences in powder densities and surface areas (Fig. 4-4f). Powder particles with a low density and a high surface area behave like very fine particles and thus do not flow easily compared to dense particle of the same grain-size distribution. As a consequence the deposition efficiency is decreased and porous coatings are produced.

4.3 Momentum Transfer

4.3.1 Connected Energy Transmission

As mentioned above, plasma spraying can be described as a connected energy transmission process, starting with the transfer of energy from an electric potential field to

the plasma gas (plasma heating), proceeding with the transfer of energy (momentum and heat transfer) from the plasma to the powder particles, and concluding with the transfer of energy from the particles to the substrate.

In the following section, principles of momentum transfer and modeling will be discussed. Particles are being accelerated in the plasma jet. The process can be described by a two-phase fluid flow, but is much more complex because of the presence of charged particles, chemical reactions, and large temperature gradients. Particle velocities can be measured by time-of-flight LDA (see Sect. 3.4.2.2).

4.3.2 Modeling of Momentum Transfer

Figure 4-7 shows the velocities of differently sized alumina particles in an argon/hydrogen plasma jet [10]. The larger the particles the lower is the response to the gas velocity. The 3 μm particles are used as 'tracers' to measure the velocity of the gas alone in the absence of larger particles. The gas velocity decreases continuously on exiting from the nozzle. The 18 μm particles reach a maximum velocity of $220\,\mathrm{m\,s^{-1}}$. If the target distance is 15 cm, than the particle velocity is around $170\,\mathrm{m\,s^{-1}}$, i.e. one half of the velocity of sound at atmospheric pressure in air. Larger particles, like the 46 μm particles reach a maximum of only $140\,\mathrm{m\,s^{-1}}$ but this velocity does not decay quickly because of the high inertia of the large particles.

Momentum transfer from the plasma to the particles can be modeled with the following assumptions:

- the molten droplets are spherical,
- the molten droplets are carried in a gas stream with constant temperatures along its symmetry axis,
- the gas jet is not influenced by particles, i.e. operation is carried out in a diluted system as opposed to dense loading conditions (see Sect. 4.4.3), and
- continuum gas flow.

The governing equation applied to decribe the impulse (momentum) transfer is the Basset–Boussinesq–Oseen equation of motion[1]. This equation determines the time dependency of the particle velocity, $\mathrm{d}V_\mathrm{p}/\mathrm{d}t$, considering only the viscous drag force, F_D and the velocity gradient, $V_\mathrm{g} - V_\mathrm{p}$:

$$\mathrm{d}V_\mathrm{p}/\mathrm{d}t = V_\mathrm{p}(\partial V_\mathrm{p}/\partial x) = [3C_\mathrm{D}\rho_\mathrm{g}/4d_\mathrm{p}\rho_\mathrm{p}]|V_\mathrm{g} - V_\mathrm{p}|(V_\mathrm{g} - V_\mathrm{p}) \qquad (4\text{-}1)$$

---

[1] The equation given here is a simplification. The complete equation of motion of a particle injected into a plasma jet can be described in a summary form by $F_\mathrm{P} = F_\mathrm{D} + F_\mathrm{PG} + F_\mathrm{AM} + F_\mathrm{H} + F_\mathrm{E}$, where F_P = mass–acceleration product, i.e. particle inertia, F_D = Stokesian drag force, F_FG = drag due to the plasma pressure gradient, F_AM = drag due to the added mass, F_H = Basset history term due to the nonsteady motion of the particle, and F_E = external potential forces such as gravity, electric or magnetic forces [11]. Since in a thermal plasma the density of the gas is rather low compared to that of the particle, all terms but the viscous drag force F_D and the history term F_H may be neglected. Thus the equation reduces to $F_\mathrm{P} = F_\mathrm{D} + F_\mathrm{H}$. This applies essentially to pure Stokesian motion with low Reynolds numbers ($C_\mathrm{D} = 24/\mathrm{Re}$). According to Pfender [12] additional turbulence and thermophoretic effects must be considered.
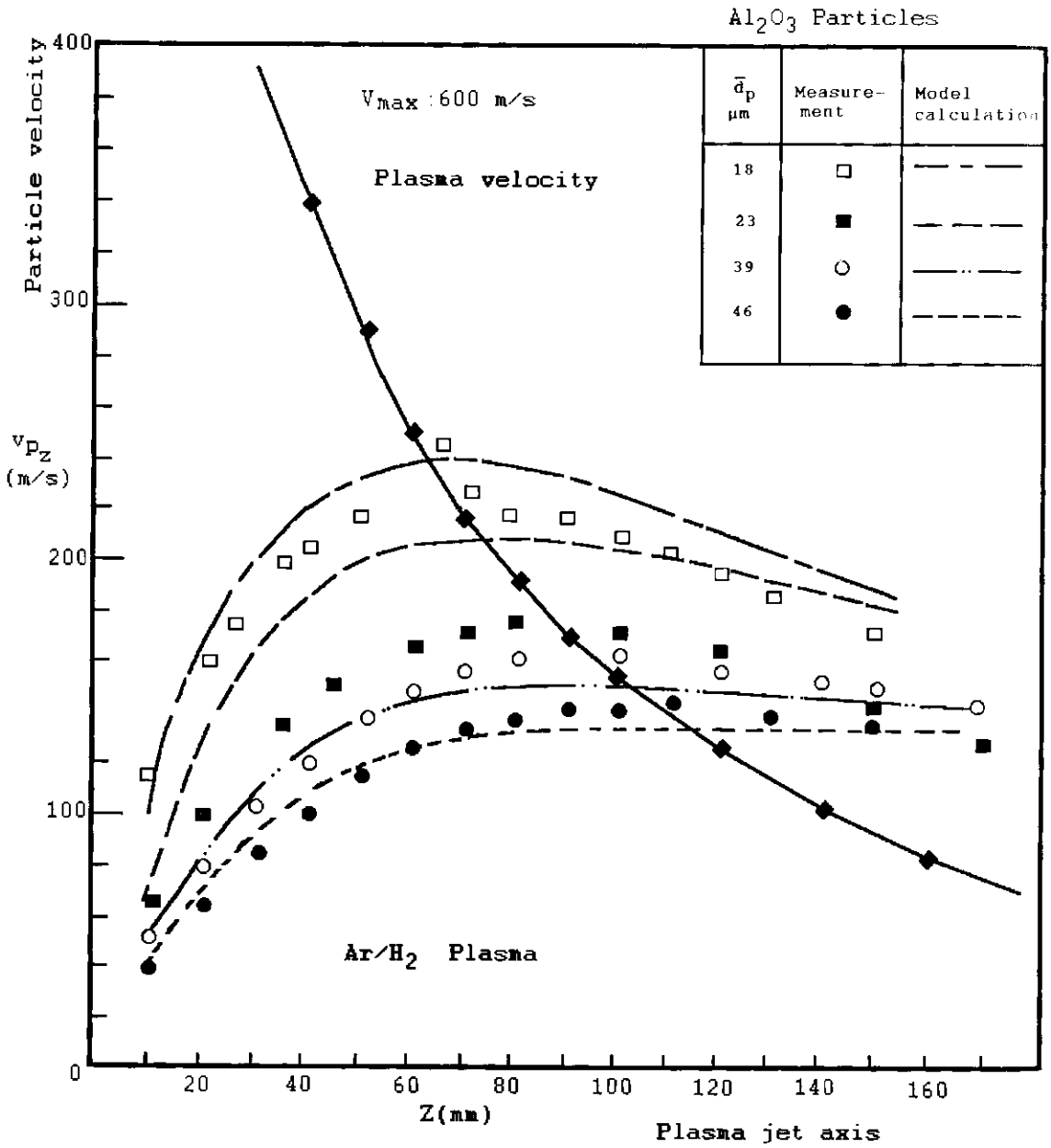
Figure 4-7. Transfer of plasma velocity to alumina particles of different sizes [10].

where

$$C_D = [F_D/A_p]/[1/2\rho_g u_R^2] \tag{4-2}$$

with d_p being the particle diameter and A_p the cross-sectional area of the particle. The velocity term $u_R = V_g - V_p$, i.e. the relative velocity of a particle with respect to the plasma gas can be more accurately described by considering the velocity components of the particle in axial (z) and radial (r) directions: $u_R = [(V_g^{(z)} - V_p^{(z)})^2 + (V_g^{(r)} - V_p^{(r)})^2]^{1/2}$.

The decay of the plasma velocity V_g with distance from the nozzle exit is inversely proportional to the distance x, and can hence be described by the simple relation

$$V_g = V_0/(c_1 + c_2 x), \tag{4-3}$$

where V_0 is the exit velocity, and c_1, c_2 are constants.

A semiempirical approach to the particle velocity in a plasma jet was developed by Nikolaev [13] for a Reynolds number Re < 1

$$V_p = V_g\{1 - \exp[18\nu\rho_g t/(d_p^2 \rho_m)]\}, \tag{4-4a}$$

with $\nu =$ kinematic viscosity of the plasma, $\rho_g =$ plasma gas density, $\rho_m =$ particle density, and $t =$ dwell time of the particle, and for Re > 2

$$V_p = (V_g t)/t^* + t; \quad t^* = 4d_p\nu/3C_D v_g \rho_m. \tag{4-4b}$$

4.3.3 Estimation of the Drag Coefficient

The viscous drag coefficient C_D has been evaluated for different Reynolds numbers ranging from $C_D = 24/\text{Re}$ for $0 < \text{Re} < 0.2$ (Stokesian motion) to $C_D = (24/\text{Re})(1 + 0.189\,\text{Re}^{0.63})$ for $21 \le \text{Re} \le 200$ [14]. An expression for higher turbulent plasmas ($0.15 \le \text{Re} \le 500$) was given as $C_D = (23.7/\text{Re})[1 + 0.165\,\text{Re}^{2/3} - 0.05\,\text{Re}^{-0.1}]$ [15]. It should be noted that there are problems with modeling the forces acting on a particle in a plasma jet that require modification of the Basset–Boussinesq–Oseen approximation. These problems relate to (1) the large temperature gradient present, (2) the change of the particle diameter d_p and thus the projected surface area by surface ablation (see 4.3.4), thermal expansion, decomposition and vaporization, and (3) noncontinuum effects for small particles with $d_p < 10\,\mu\text{m}$.

1. Corrections for temperature effects have been made by Lewis and Gauvin [11] who modified the drag coefficient assuming a local Reynolds number

$$C_D = C_{Df}\left[(\rho_\infty/\rho_f)(\nu_f/\nu_\infty)^{0.15}\right], \tag{4-5}$$

with $C_{Df} =$ drag coefficient evaluated at the 'mean film temperature' ($T_f = (T_\infty - T_s)/2$), $\rho_f =$ gas density at T_f, $\rho_\infty =$ gas density at T_∞, $\nu_f =$ kinematic vis-

cosity at T_f, and v_∞ = kinematic viscosity at T_∞. Another correction approach was reported by Lee *et al.* [16] with

$$C_\mathrm{D} = C_\mathrm{Df}[\rho_\infty \mu_\infty / \rho_s \mu_s]^{-0.45} = C_\mathrm{Df}(v_\infty / v_s)^{-0.45} = C_\mathrm{Df} f_1 \tag{4-6}$$

where the subscripts ∞ and s refer to the plasma temperature, T_∞ and the surface temperature of the particle, T_s, respectively.

2. The drag coefficient is according to Eq. 4-2 dependent on the projected surface area of the particle perpendicular to the flow, A_p. When the particle diameter decreases by ablation or evaporation, the surface area also decreases, and the drag coefficient and hence the drag force change accordingly.

3. Noncontinuum effects for small particles ($d_\mathrm{p} < 10\,\mu\mathrm{m}$) can be accounted for through the Knudsen number, $\mathrm{Kn} = (\lambda / d_\mathrm{p})$, where λ = molecular mean free path. In the slip flow regime $0.01 < \mathrm{Kn} < 1$, a correction of the drag coefficient has been proposed [17] as

$$C_\mathrm{D,slip} = C_\mathrm{D,cont}[1/(1 + AB(4\,\mathrm{Kn}/\mathrm{Pr}))]^{0.45} = C_\mathrm{D,cont} f_2 \tag{4-7}$$

where $A = (2 - a)/a$ with a = thermal accommodation coefficient, $B = (\gamma/1 + \gamma)$ with $\gamma = c_\mathrm{p}/c_\mathrm{v}$, and Pr = Prandtl number. According to Pfender [12] the corrections expressed in Eqs. 4-6 and 4-7 can be combined and a general expression for the drag coefficient is obtained:

$$C_\mathrm{D} = C_\mathrm{Df} f_1 f_2. \tag{4-7a}$$

The acceleration of the particles caused by the viscous drag forces is proportional to the relative velocity of the particles, and inversely proportional to the density and the square of the diameter of the particle. The correction for noncontinuous effects is particularly important for low-pressure plasma spraying where the mean free path of the gas molecules, λ is close to the diameter of the particles, d_p.

Figure 4-8 shows the dependency of the viscous drag coefficient, C_D expressed in Eq. 4-2 as a function of the Reynolds number. It can be seen that the standard drag curve is limited by the Stokes equation for low Reynolds numbers, i.e. laminar flow regime, whereas it is limited by Newton's law at high Reynolds numbers, i.e. turbulent flow regime as present in most plasma arc jets. The turbulent flow causes a nonsteady flow field around the immersed particles and thus a rapid change of the particle Reynolds number with time. According to Lewis and Gauvin [11] this results in an excess drag that was predicted to range from 20% for $30\,\mu\mathrm{m}$ particles to 100% for $150\,\mu\mathrm{m}$ particles. Together with the effect of the Basset history term the effect of excess drag must be considered in momentum transfer modeling.

4.3.4 Surface Ablation of Particles

For liquid or plastically deformable material a global approximation of the force balance on the side walls of the deforming particle is

$$(4\pi r^2)(C_\mathrm{D} \rho_\mathrm{p} v^2/4) \approx m(\mathrm{d}^2 r/\mathrm{d}t^2), \tag{4-8}$$

The figure shows C_D plotted against N_{Re} with regions labeled laminar, turbulent, Stokes Law ($C_D = 24/N_{Re}$), Newton, and Standard drag curve.
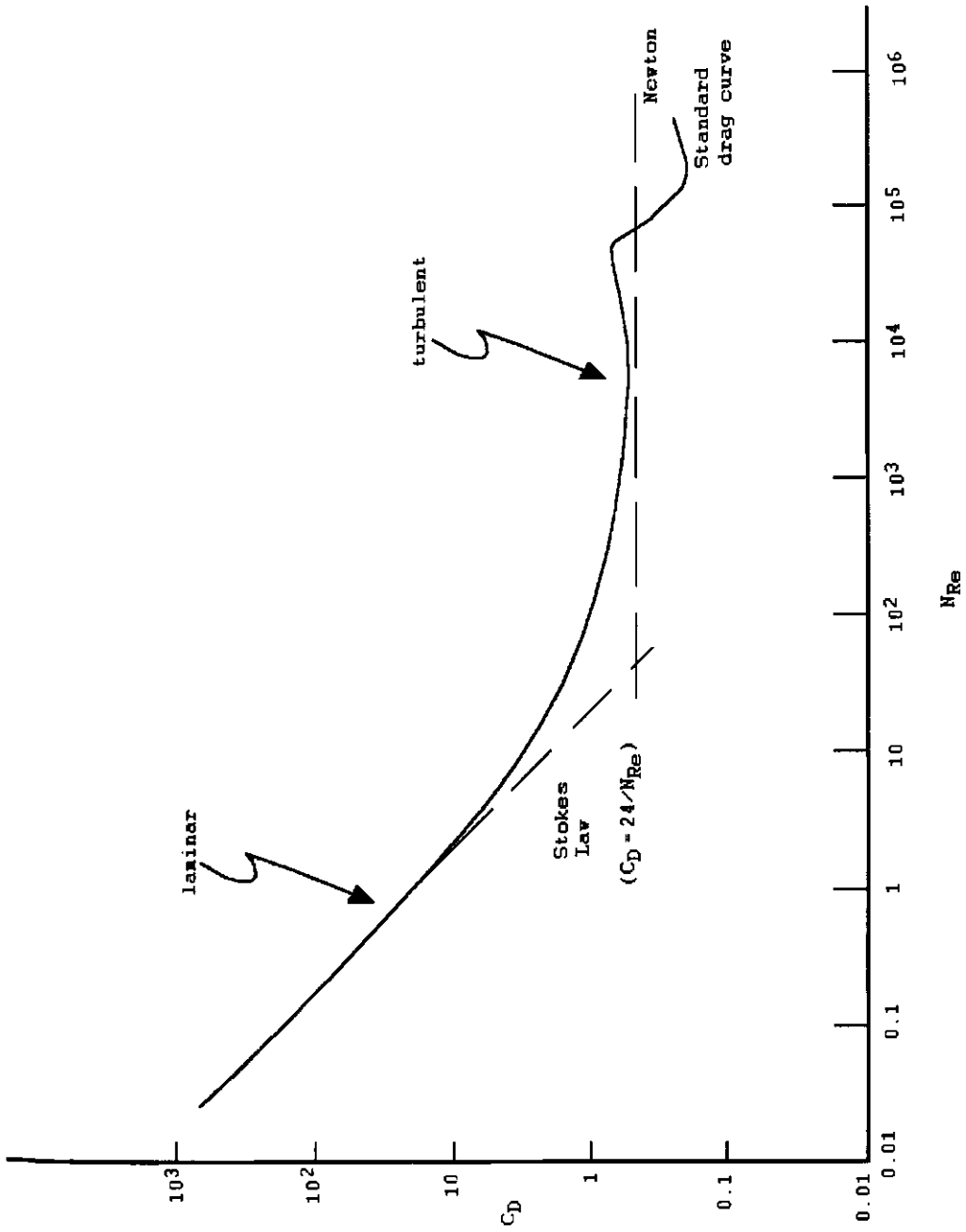
Figure 4-8. Dependence of the viscous drag coefficient C_D on the Reynolds number.

where C_D = drag coefficient, ρ_p = density of plasma gas, v = particle velocity, m = particle mass and r = particle radius.

Assuming the density of the material, ρ_m remains constant, the expression

$$r(d^2r/dt^2) = C_D\rho_p v^2/2\rho_m \tag{4-9}$$

can de derived. The surface of the sphere is heated by convection and it is shed by ablation. The resulting mass change is

$$Q_A(dm/dt) = -(1/2)h\rho_p A_p v^3, \tag{4-10}$$

where Q_A = heat of ablation, and h = heat transfer coefficient. It can be seen that the mass change is proportional to the third power of the particle velocity and thus the materials loss becomes significant at high velocities. Also, the maximum ablation rate can be determined [18] from

$$Q_A(dm/dt) \approx A\sigma T^4, \tag{4-11}$$

and finally

$$Q_A(dm/dt) = -A_p \min[(h/2)\rho_p v^3, \sigma T^4]. \tag{4-12}$$

4.4 Heat Transfer

4.4.1 Heat Transfer under Low Loading Conditions

If the mass of powder particles injected into a plasma jet is small enough not disturb the flow of the plasma and to cool it down by radiative losses, the heat transfer can be estimated under simplifying assumptions. In particular, the Navier–Stokes equations (see Sect. 4.4.3) for the flow around a sphere are highly nonlinear even under the simplifying assumptions made above, i.e. for constant physical property plasmas. Thus no completely exact solutions exist for these equations [19].

In many cases an analytical solution is not available, and only numerical models can be used successfully. As shown in Fig. 4-9, a particle in contact with a heated plasma jet acquires energy by convective (and conductive) processes, q_c and loses energy to the surroundings by radiation, q_r. The net energy contribution to the heating and melting of particles is the difference between these two values (Eq. 4-18).

The amount of heat gained by convective energy transfer from the plasma to the particle is

$$q_c = ha(T_\infty - T_s), \tag{4-13}$$

the amount of heat lost by radiative energy transfer to the surrounding is

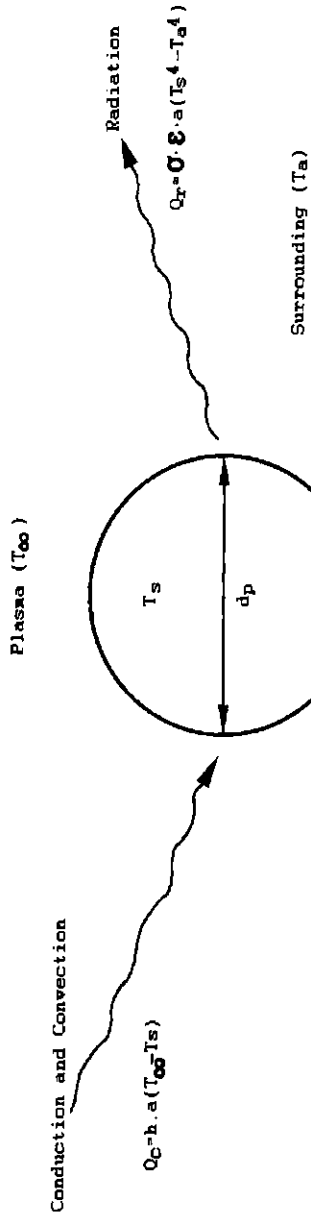$$q_r = \sigma\varepsilon a(T_s^4 - T_a^4), \tag{4-14}$$

Figure 4-9. Heat transfer equilibrium of a powder particle in a plasma.

where h = plasma/particle convective heat transfer coefficient, a = surface area of the particle, T_∞ = free-stream plasma temperature, T_s = particle surface temperature, T_a = temperature of the surrounding, σ = Stefan–Boltzmann constant, and ε = particle emissivity.

The heat transfer coefficient can be expressed as

$$h = k_f \, Nu/d_p, \tag{4-15}$$

where $k_f = C_g \eta / Pr$, or $h = [C_g \eta / d_p][Nu/Pr]$ (see Appendix A).

The symbols Nu and Pr denote the Nusselt and Prantl numbers, and k_f is the thermal conductivity of the particles. C_g, d_p and η are, respectively the specific heat of the plasma gas, the particle diameter and the gas viscosity.

The choice of the numerical value of the Nusselt number is crucial for a realistic estimate of the heat transfer rates from the plasma to the particles in the same way the choice of the drag coefficient is important for the momentum transfer. For the heat transfer between a gas and a spherical particle the expression

$$Nu = 2.0 + b \, Re^m \, Pr^n \tag{4-16}$$

was given by Frösling [20], and Raithby and Eckert [21], and later used by Sayegh and Gauvin ($b = 0.473$, $m = 0.552$, $n = 0.78 \, Re^{-0.145}$) [19][2] and Vardelle *et al.* ($b = 0.6$, $m = 0.6$, $n = 0.33$) [22]. Other more complex expressions for Nu were introduced by Fiszdon [15], Lee *et al.* [16] and Lewis and Gauvin [11]. Also, noncontinuum effects in heat transfer over the range of the Knudsen number $0.01 < Kn < 1.0$ have been proposed by Chen and Pfender [23] as

$$q_{noncont} = q_{cont}[1/\{1 + (2Z^*/d_p)\}], \tag{4-17}$$

with Z^* = temperature 'jump' distance. Because the particle size is of the same order of magnitude as the molecular mean free path length in the plasma gas, this 'rarefaction effect' [12] may exert a strong influence on the heat transfer.

The net energy acquired by a particle in a plasma is obtained from Eqs. 4-13 and 4-14 as

$$q_n = q_c - q_r \gg 0, \tag{4-18}$$

since q_r is generally small compared to q_c because of the small value of the Stefan–Boltzmann constant $\sigma = 5.67 \times 10^{-8} \, W \, m^{-2} \, K^{-4}$.

The requirement for an efficient energy economy during the plasma spray operation is that all particles melt completely during their very short residence time in the plasma jet. This means that the total energy received by the particles, q_n must be

---

[2] Actually, instead of the limiting Nusselt number of 2 an expression $2f_0 = \{2(1 - [T_w/T_\infty]^{1+x}\}/\{(1 + x)/(1 - [T_w/T_\infty])(T_w/T_\infty)^x\}$ with $x = 0.8$ was used, where T_w is the surface temperature of the particle and T_∞ is the plasma temperature.

equal to or larger than the energy required to melt the particles. This energy quantity consists of two components: the energy needed to heat the particles from their initial temperature to their melting point and the latent heat of fusion.

$$\int_0^\tau q_n \, dt > \sum \{m_p c_p (T_m - T_0) + m_p H_m\},\tag{4-19}$$

where m_p = mass of particle, c_p = specific heat of particle, T_m = melting point, T_0 = initial temperature, H_m = latent heat of fusion and τ = residence time of the particle in the plasma jet.

Normally, superheating is required to achieve sufficiently high temperatures of the particles, and to decrease the viscosity of the liquid droplet. The degree of super-heating depends on the Biot number, which is the ratio of the thermal conductivity of the plasma gas, k_g to the thermal conductivity of the particles, k_p:

$$Bi = k_g/k_p.\tag{4-20}$$

The requirement of a uniform particle temperature implies that $Bi < 0.01$, i.e. the thermal conductivity of the particle material has to be much higher than that of the plasma gas. Thus the numerical value of the Biot number can be used to determine *a priori* whether large temperature differences may occur between the surface and the center of a (spherical) particle that may compromize the conjecture of a uniform temperature distribution and thus uniform melting behavior. According to Bourdin *et al.* [24], a characteristic temperature $T^* = \Delta T_s/(T_\infty - T_s) = f(Bi)$ can be defined. For $Bi < 0.02$, the temperature between the surface and the center of the particle becomes less than 5% of $(T_\infty - T_s)$.

Porous particles and particles with low thermal conductivity will develop large internal temperature gradients that can often exceed 1 000 K. Figure 4-10 shows the temperature history of alumina particles of 50 µm radius at a plasma temperature of 10 000 K in hydrogen, nitrogen and argon plasmas [24]. The left lines depict the particle surface temperature, the right lines the temperature at the center of the particles. The temperature difference depends strongly on the heat flux to the particle. For example, the temperature difference in a hydrogen plasma can be so high that the thermal stresses induced can lead to shattering of the particles. As is obvious from Fig. 4-10, the radial temperature differences across a particle are quite large for a hydrogen plasma, and decrease for a nitrogen and even more for an argon plasma. This is because of the large differences in the thermal conductivities, k_g of the plasma gas, being 4.6, 1.6 and 0.2 W m^{-1} K^{-1} for hydrogen, nitrogen and argon, respectively. The value of the thermal conductivity influences the particle surface temperature because the solution of the equation

$$dT_s/dt = -12k_g(T_s - T_\infty)/\rho_s c_s d_p^2\tag{4-21}$$

($Nu = 2$, i.e. only conductive heat transfer, $q_r = 0$, i.e. no radiative heat losses) is

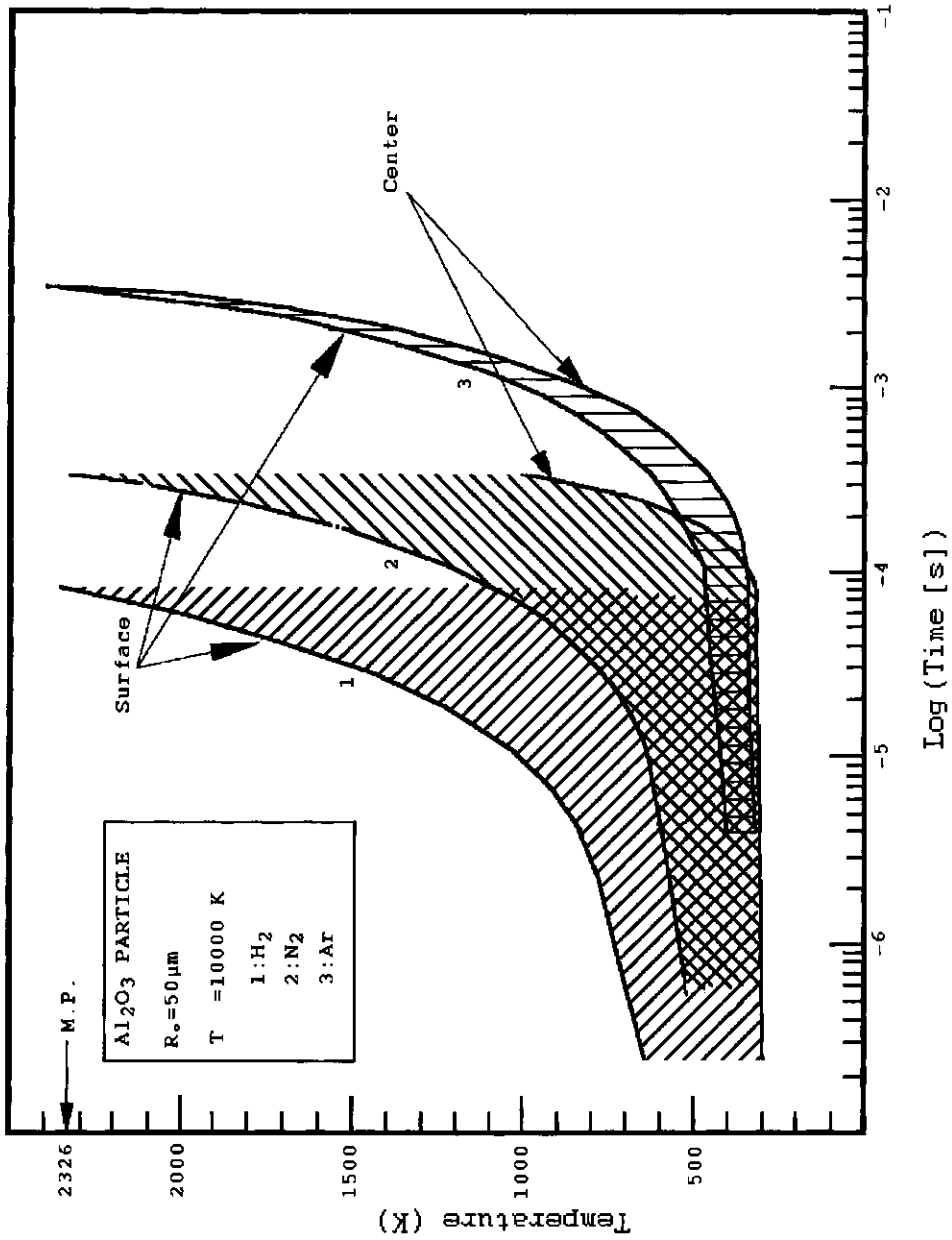$$(T_s - T_\infty)/(T_0 - T_\infty) = \exp[12k_g t/\rho_s c_s d_p^2],\tag{4-22}$$

Figure 4-10. Temperature history of 50 μm-alumina particles at a temperature of 10000 K in hydrogen (1), nitrogen (2) and argon (3) plasmas [24].
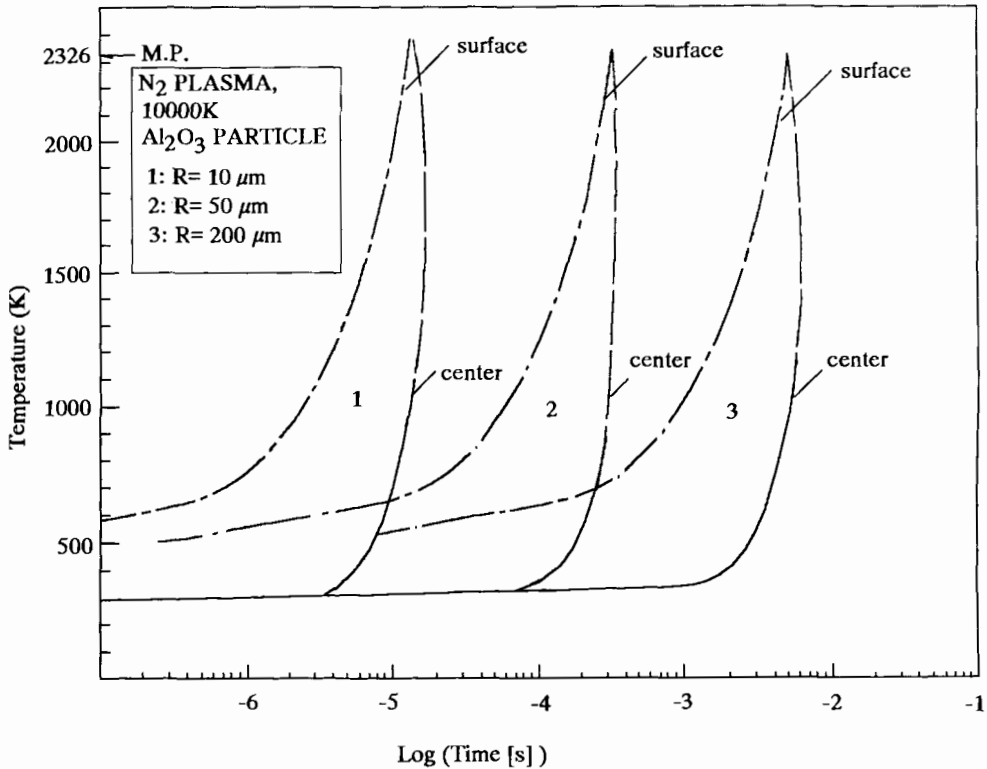
Figure 4-11. Temperature history of alumina particles of different radii suddenly immersed in a nitrogen plasma at 10 000 K [24].

where ρ_s and c_s are the density and the specific heat, respectively of the particle, d_p the particle diameter, and T_0 and T_∞ the temperature of the surrounding and the plasma, respectively [24]. From Fig. 4-10 it can be seen that the time required to melt an alumina particle of 50 μm radius ranges from 80 μs (hydrogen plasma) to 0.3 ms (nitrogen plasma) to 4 ms (argon plasma).

Figure 4-11 shows the temperature history of alumina particles of different radii (10, 50 and 200 μm) suddenly immersed in a nitrogen plasma at 10 000 K [24]. Again, the leading curves refer to the surface temperature of the particle, the trailing curves to the center of the particles. The radius of the particles has little influence on T_s.

A somewhat easier approach to make a qualititive estimate of the materials performance in terms of ease of plasma melting of particles is to consider the maximum particle diameter for complete melting, d_{max}. This is a useful parameter for comparing materials with widely differing densities and thermophysical properties.

Based on the equation of transient heat conduction in solid spheres (assumption: surface of particle is brought instantaneously to its melting point), the following expression can be evaluated [25]:

$$(T_m - T_R)/(T_m - T_I) = f(Bi, Fo) = f[hr/k, \alpha\Theta/r^2], \qquad (4\text{-}23)$$

Table 4-2. Relative ease of plasma spraying for various oxide, carbide and metallic coatings [25].

Material	Thermal diffusivity, a [cm^2 s^{-1}]	$C_p(T_m - T_i)$ [cal g^{-1}]	d_{max}[a] [μm]	Relative ease of plasma spraying
ZrO$_2$	0.005	430	26	5
UO$_2$	0.025	214	58	4
TiC	0.04	645	72	3
TaC	0.09	115	110	1
ZrC	0.05	525	82	3
TiN	0.07	556	96	2
B$_4$C	0.06	109	90	2
Steel 304	0.05	226	82	3
W	0.63	111	280	1

[a] $d_{max} = 2[a\Theta/0.3]^{1/2}$ for $\Theta = 10^{-4}$ s

Table 4-3. 'Ease of melting' parameter, Φ, according to Marynowski [27].

	Material	Φ	T_m(K)	ρ(g cm^{-3})
Difficult	TiC	1.53	3.410	4.93
Carbides,	TiN	1.40	3.200	5.21
Nitrides	ZrC	1.58	3.840	6.73
Easier	ZrO$_2$	1.38	2.700	4.40
	Al$_2$O$_3$	1.26	2.318	3.97
Oxides	TaC	1.09	4.150	14.53
	SiO$_2$	1.21	1.975	2.65
Easy	Ni	0.58	1.728	8.90
	Ta	0.80	3.270	16.60
Metal	W	0.83	3.650	19.30
	Mo	0.90	2.883	10.20

where T_m = melting point of material, $T_R = T$ at points along the radius of a sphere ($r = 0$ at center, $r = r_0$ at surface), T_i = initial temperature of particle, α = thermal diffusivity = $k_p/\rho c_p$, Θ = time, Bi = Biot number and Fo = Fourier number.

At the particle center ($r = 0$), the equation becomes approximately

$$1 - (T_0/T_m) = \Phi\{hr_0/k, \alpha\Theta/r_0^2\}. \tag{4-24}$$

A comparison of different materials in terms of the relative ease of plasma spraying is given in Table 4-2. Assuming constant time (100 μs), a center temperature of the particle $T_0 = 0.9T_m$, a Biot number of 10, and a Fourier number of 0.3, an ex-

pression can be obtained for the maximum diameter of a particle that completely melts in 100 μs:

$$d_{max} = 2r_0 = 2[\alpha\Theta/0.3]^{1/2}. \tag{4-25}$$

For a qualitative comparision of the melting behavior of different materials Marynowski [26] introduced an 'ease of melting' parameter $\Phi = 10^{-3}T_m/\rho^{1/2}$. Easy to melt materials have $\Phi < 1.0$, difficult to melt materials $\Phi > 1.4$ (see Table 4-3). The parameter Φ is based on considerations by Engelke [27] involving equating the time required for the particle to traverse the plasma of length X to the time required to melt this particle completely. An expression can be evaluated that leads to

$$[X(k_p\Delta T)^2/V\mu] \geq [L^2D^2/16\rho], \tag{4-25a}$$

where k_p = mean boundary layer thermal conductivity, V = plasma velocity, μ = plasma viscosity, L = particle heat content, D = particle diameter, and ρ = particle density. Since the left hand side of Eq. 4-25a increases proportionally to the square of the plasma enthalpy it follows that the enthalpy should be proportional to $(LD/\rho^{1/2})$ [27].

4.4.2 Exact Solution of Heat Transfer Equations

According to Chen and Pfender [28] exact solutions for the heat transfer from a plasma to a particle under low-loading conditions can be obtained considering the following simplifying assumptions:

- particles are exposed to a uniform atmospheric pressure argon plasma,
- heat transfer process is steady,
- spherical particles,
- free convection neglected (Re = 0, Gr ≪ 1),
- radiation from and to particle neglected (St = 0), and
- influence of vapor from evaporating particles neglected.

Two cases can be distinguished: heating of a particle without evaporation, and with evaporation. However, realistically a certain degree of vaporization of material below the boiling point has always to be taken into account. As the temperature of a particle in the plasma jet increases its vapor pressure also increases. Then the mass loss by vaporization [12] becomes

$$dm/dt = \rho h_m M \ln(p/p - p_v), \tag{4-26}$$

where h_m = mass transfer coefficient, M = molecular weight of the material, p = partial vapor pressure with respect to saturation, and p_v = partial vapor pressure with respect to the particle surface temperature. The mass transfer coefficient can be

expressed similarly to the Nusselt number (Eq. 4-15) by related dimensionless groups as

$$\text{Sh} = h_m d_p / D_{ij} = 2.0 + 0.6\,\text{Re}^{0.5}\,\text{Sc}^{0.33}, \tag{4-27}$$

with Sh = Sherwood number, Re = Reynolds number, Sc = Schmidt number, d_p = particle diameter and D_{ij} = interdiffusion coefficient [12].

4.4.2.1 Particle Heating without Evaporation

The simplified heat transfer equation is

$$4\pi r^2 (k\,dh/c_p\,dr) = Q_0 \tag{4-28}$$

where k = thermal conductivity, c_p = specific heat, h = specific enthalpy of plasma and r = radial coordinate.

Introducing the 'heat conduction potential', S, as

$$S = \int_{T_0}^{T} k\,dT = \int_{h_0}^{h} (k/c_p)\,dh, \tag{4-29}$$

Eq. (4-28) can be rewritten as

$$Q_0 = 4\pi r_s^2\,dS/dr \tag{4-28a}$$

and on integration

$$Q_0 = 4\pi r_s (S_\infty - S_s), \tag{4-30}$$

where S_∞ and S_s are the values of S at the surface and far away from the surface, and r_s is the particle radius.

The specific heat flux is $q_0 = Q_0/4\pi r_s^2$, and thus

$$q_0 = (S_\infty - S_s)/r_s. \tag{4-31}$$

It can be seen that the specific heat flux is inversely proportional to the particle radius.

The Nusselt number is defined as

$$\text{Nu} = q_0 2 r_s /(S_\infty - S_s) = (h d_p)/k_f \tag{4-32}$$

Under pure heat conduction condition (Re = 0), Nu = 2. For Re $\neq 0$ follows

$$\text{Nu} = q_0 2 r_s /k(T_\infty - T_s) = q_0 2 r_s /(k c_p)(h_\infty - h_s). \tag{4-32a}$$

From Eq. 4-29 it follows that S is only a function of the temperature for a given plasma gas and a given solid material. Figure 4-12 relates the thermal conductivities of the plasma gases argon, nitrogen and hydrogen and the heat conduction potentials as functions of the plasma temperature [24]. Figure 4-13 shows in addition the plot of the heat conduction potential, S, of an argon/hydrogen mixture as a function

Figure 4-12. Thermal conductivities $k(T)$ (a) and heat conduction potentials $I(T)$ (b) of some pure plasma gases [24].
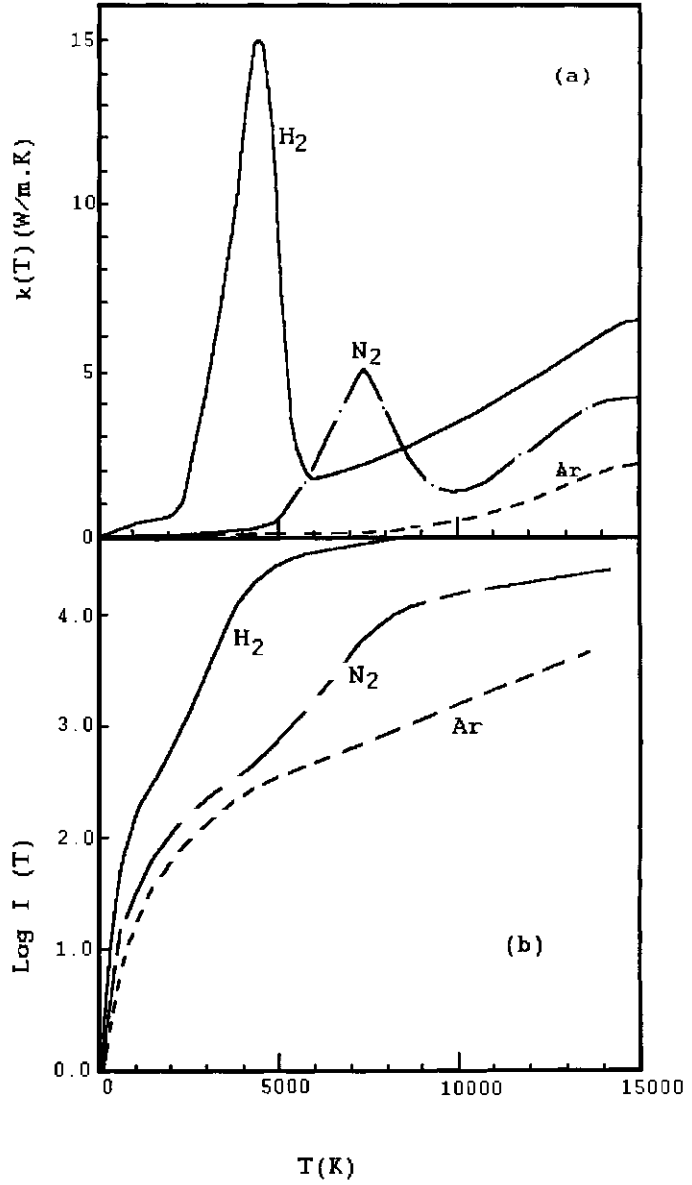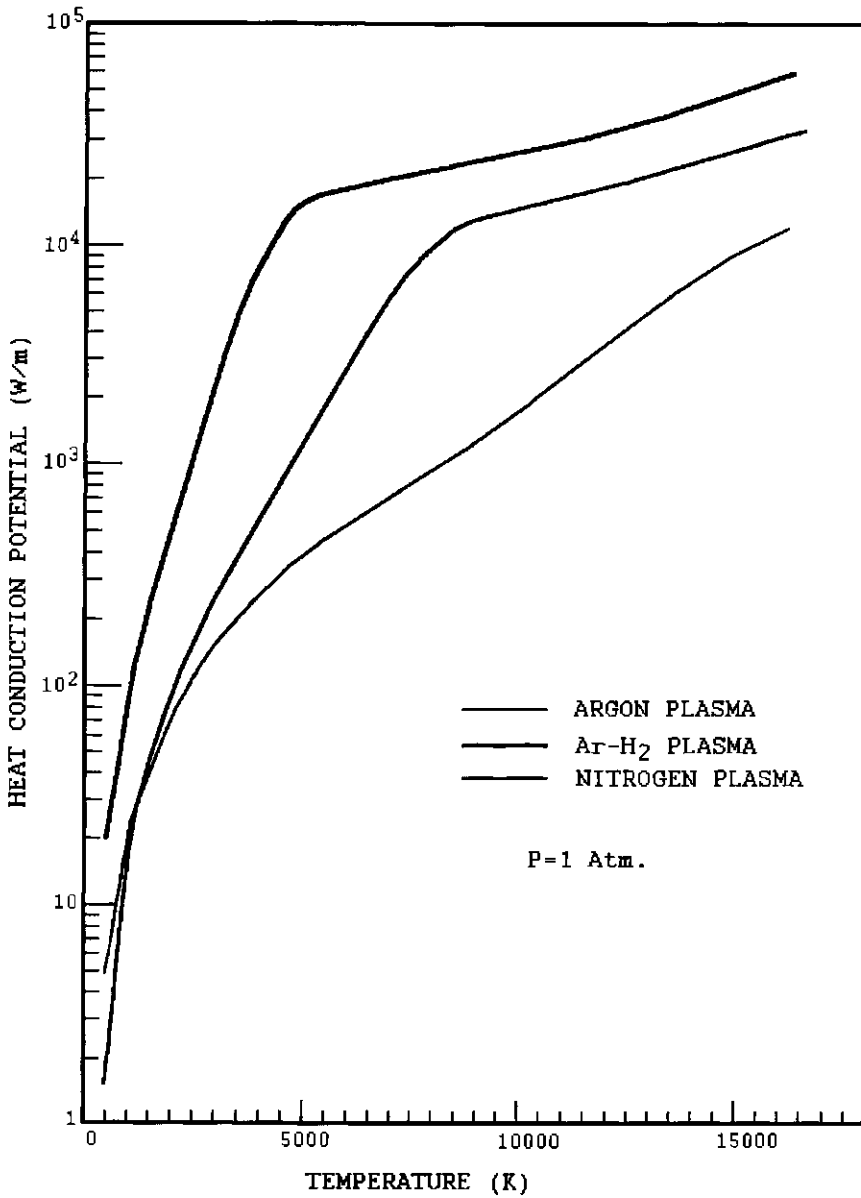
Figure 4.13. Heat conduction potentials of pure (argon, nitrogen) and mixed (argon/hydrogen) plasmas at atmospheric pressure [28].

of the plasma temperature. The high thermal conductivity of the added hydrogen leads to a substantially increased heat conduction potential of the mixture compared to pure argon. For this reason argon/hydrogen mixtures are frequently used as a plasma gas to improve the melting characteristics of powders with high melting points such as zirconia.

4.4.2.2 Particle Heating with Evaporation

The simplified convection–diffusion equation can be written as

$$-4\pi r^2 D\rho \, \mathrm{d}f/\mathrm{d}r + Gf = G \tag{4-33}$$

or

$$4\pi r^2 D\rho \, \mathrm{d}f/\mathrm{d}r = G(f - 1) \tag{4-33a}$$

where G = total mass flux due to evaporation, f = mass fraction of evaporated species, D = diffusion coefficient and ρ = gas density. Boundary conditions are $f = 0$ as $r \rightarrow \infty$.

The related energy equation is

$$4\pi r^2 (k/c_p)(\mathrm{d}h/\mathrm{d}r) = G(h - h_s + L), \tag{4-34}$$

where h = enthalpy corresponding to the surface of particle and L = latent heat of evaporation. Boundary conditions for solving Eq. 4-34 are

$$r = r_s \quad h = h_s$$

$$r \rightarrow \infty \quad h = h_\infty$$

The solution of Eq. 4-34 is

$$G = 4\pi r_s \int (k/c_p)(\mathrm{d}h/h - h_s + L) = 4\pi r_s \int (k \, \mathrm{d}T)/h - h_s + L. \tag{4-35}$$

The total mass flow rate is related to the total heat flux by

$$Q_1 = GL. \tag{4-36}$$

Therefore:

$$Q_1 = 4\pi r_s L \int (k \, \mathrm{d}T)/h - h_s + L, \tag{4-37}$$

and, because $q = Q/4\pi r^2$, the specific heat flux becomes

$$q_1 = (L/r_s) \int (k \, \mathrm{d}T)/h - h_s + L. \tag{4-37a}$$
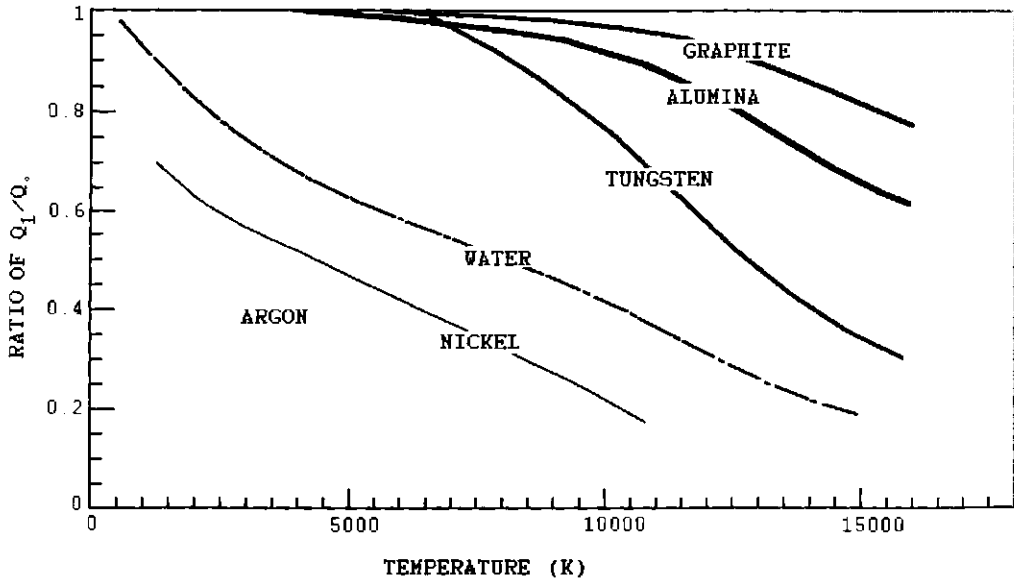
Figure 4-14. Heat flux ratios Q_1/Q of different materials as a function of the argon plasma temperature [28].

Since the integral is only a function of T for a given plasma gas and a given material it can be replaced by the function

$$\int (k \, dT)/h - h_s + L = M(T_\infty, T_s, L). \tag{4-38}$$

From Eqs. 4-31 and 4-37a, the ratio of the heat flux with and without evaporation becomes

$$q_1/q_0 = (L/S_\infty - S_s)M(T_\infty, T_s, L). \tag{4-39}$$

Figure 4-14 shows a plot of q_1/q_0 as a function of the plasma temperature for different materials. It can be seen that evaporation has a strong effect if the plasma temperature is high, and if the material has a low latent heat of evaporation.

4.4.2.3 Evaporation Time of a Particle

For quasi-steady state evaporation it follows that

$$Q_1 = 4\pi r_s^2(-dr_s/dt)\rho_c L \tag{4-40}$$

or

$$q_1 = -\rho_c L(dr_s/dt). \tag{4-40a}$$

With Eq. (4-40a), (4-37a) and (4-38) one obtains

$$q_1 = (L/r_s)M(T_\infty, T_s, L) = -\rho_c L(dr_s/dt) \tag{4-41}$$

or

$$-(dr_s^2/dt) = K \tag{4-42}$$

where $K = 2M(T_\infty, T_s, L)/\rho_c$ is the so-called *evaporation constant*. This constant is only a function of temperature, not a function of the radius of the particle. Figure 4-15 shows the evaporation constant K for several materials as a function of the plasma temperature.

The integration of Eq. (4-42) leads to

$$r_{s0}^2 - r_s^2 = Kt \tag{4-43}$$

where r_{s0} is the initial radius of the droplet at $t = 0$.

The time for complete evaporation of a droplet ($r_s = 0$) becomes then

$$t_V = r_{s0}^2/K. \tag{4-44}$$

This time does not include the time needed for initial heating and melting of the particle. From Fig. 4-15 we obtain for an alumina particle of a radius $r = 50\,\mu\text{m}$, heated in an argon plasma of $T_\infty = 10\,000\,\text{K}$ the time for complete evaporation $t_V = (5.0 \times 10^{-5})^2/(3.0 \times 10^{-8}) = 80\,\text{ms}$. From this result it is obviously necessary to design the plasmatron nozzle and to set the spray parameters in such a way that the residence time of a $50\,\mu\text{m}$-alumina particle in the $10\,000\,\text{K}$-zone of the plasma jet is much shorter than $80\,\text{ms}$ to avoid substantial evaporation. On the other hand the dwell time must be substantially larger than the $4\,\text{ms}$ required to completely melt an alumina particle of that size as shown in Figs 4-10 and 4-11.

The evaporation of particles in the plasma gas can drastically reduce the specific heat flux in the plasma (Eq. (4-39), Fig. 4-14). On the other hand, the heat transfer calculations by Chen and Pfender [28] assumed that no influence exists on the vapor from evaporating or sublimating particles on the thermophysical properties of the plasma.

There is, however, a noticeable effect on the temperature of the plasma under dense particle loading conditions (see, for example, Proulx *et al.* [29]). Local cooling of the plasma takes place owing to the presence of particles. This will be described in the following section.

4.4.3 Heat Transfer under Dense Loading Conditions

In dilute systems, i.e. systems at low-loading conditions, it has been tacitly assumed that particle movement, including momentum and heat transfer can be considered in a ballistic manner. This means that the stochastic single-particle trajectories calculations, as well as those of the continuum flow, temperature and concentration fields can be performed under the simplifying assumptions used above. However, under realistic conditions the mass of particles injected into a plasma jet is far from those
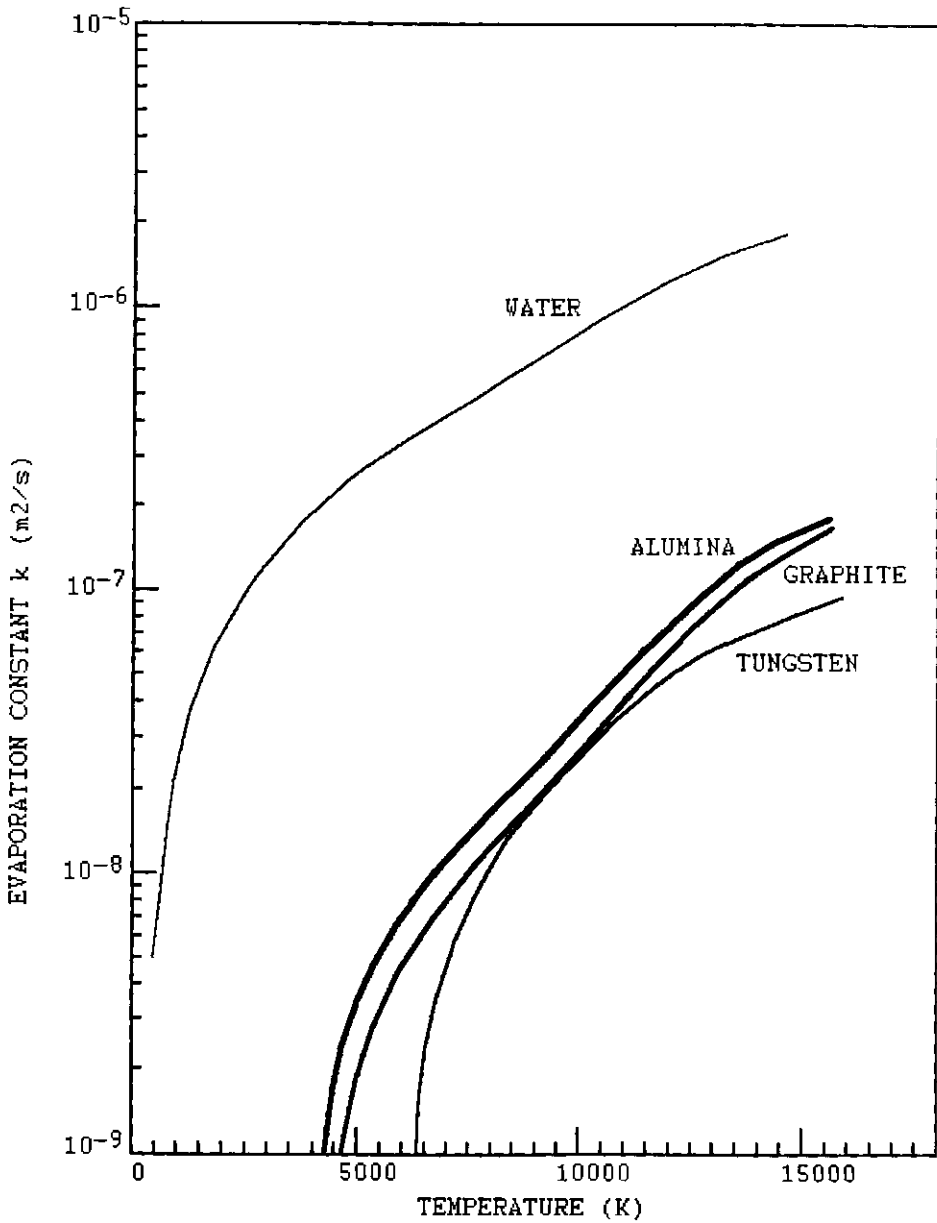
Figure 4-15. Evaporation constants for various materials in an argon plasma as a function of the plasma temperature [28].

idealized dilute systems. Indeed, in-flight processing of powders to produce plasma-sprayed coatings must be performed under high loading conditions in order to make efficient use of the thermal energy stored in the plasma. On exceeding a certain critical loading it is not warranted anymore to treat the individual impulse and thermal histories of the particles in a stochastic way. As a result particles interact with each other, and the momentum and temperature of the plasma jet will decrease with increasing mass of powder. The temperature decrease has three sources: 1. the heat extracted from the plasma to melt a larger mass of powder could cause substantial local cooling of the plasma, 2. the evaporated fraction of the powder (see Sect. 4.4.2.2) can drastically alter the thermophysical, thermodynamic and transport properties of the plasma gas, and 3. small powder particles with high optical emissivities evaporate easily, and radiate away plasma energy.

In order to arrive at an analytical solution for plasmas under dense loading conditions, the continuity, momentum, energy and species conservation equations, as well as the Maxwell electromagnetic field equations have to be solved simultaneously. This is beyond the scope of this text. Detailed descriptions of the numerical techniques employed to solve the plasma conservation equations and the electromagnetic field equations can be found in work by Mostaghimi *et al.* [30], Proulx *et al.* [29] and Crowe *et al.* [31].

4.4.3.1 Conservation Equations

To account for the particle interaction in a densely loaded plasma jet, the PSI (particle-source-in)-cell model by Crowe *et al.* [31] has been adopted by Proulx *et al.* [29]. Coupling of the stochastic single-particle trajectory calculation with those describing the continuum flow, temperature and concentration fields was obtained by introducing source–sink terms for mass, S_p^c, momentum, S_p^m (in *r*- and *z*-directions), and enthalpy, S_p^h.

The four plasma equations used to model the plasma–particle interactions under dense loading conditions [29] are

1. the continuity (mass conservation) equation

$$\mathrm{div}(\rho u) = S_p^c, \tag{4-45}$$

with $S_p^c = \sum C(\Delta m_p/\tau)$ (C = particle concentration, Δm_p = amount of mass evaporated, τ = residence time), or, in cylindrical coordinates

$$(1/r)[\delta(r\rho v)/\delta r] + \delta(\rho u)/\delta z = S_p^c. \tag{4-45a}$$

2. the momentum conservation (Navier–Stokes) equation

$$\rho u(\mathrm{grad}\ u) = -\mathrm{grad}\ p + \mathrm{div}(\eta\ \mathrm{grad}\ u) + j \times B + S_p^m, \tag{4-46}$$

with $S_p^m = \sum C[\Delta(m p v_{zp})/\tau]$ (axial direction, z) and $\sum C[\Delta(m_p v_{rp})/\tau]$ (radial direction, r).

3. the energy conservation equation

$$\rho u(\text{grad } h) = -\text{grad}(k/c_{\text{p}}) \text{ grad } h + \sigma E_\theta^2 - q_{\text{r}} + S_{\text{p}}^{\text{h}}, \qquad (4\text{-}47)$$

with $S_{\text{p}}^{\text{h}} = \sum C(q_{\text{p}} + q_{\text{v}})$, where the expression in brackets is the energy balance between convective and radiative energy transfer (see above). The term σE_θ^2 describes the energy gain of the plasma by Ohmic heating, the term q_{r} the energy loss by radiation. The source–sink term, S, can be evaluated for the local cooling generated under dense loading conditions.

4. the species conservation equation

$$\rho u(\text{grad } Y_i) = \text{div}(D \text{ grad } Y_i) + S_{\text{p}}^{\text{c}}. \qquad (4\text{-}48)$$

The general term Y_i refers to the concentration in different reference systems. In the barycentric (mass-centred) system, Y_i becomes W_i, i.e. the mass fraction of species i; in the mole-centred system, Y_i is the mole fraction, X_i, and in the volume centred system, Y_i becomes $C_i v_i$, i.e. the product of the concentration of species i and its partial molar volume.

4.4.3.2 Results of Modeling under Dense Loading Conditions

Results shown below were obtained by Proulx *et al.* [29]. The authors injected copper particles of 70 μm diameter downwards through the central tube of an inductively coupled plasmatron. Copper evaporates easily, and the vapor changes the electrical and radiative properties of argon drastically. Figure 4-16 shows the isotherms and stream lines (left) and the isocontours of the concentration of copper vapor (right) for a feed rate of 5 g min^{-1} copper powder. Since the trajectories of the particles are very close to the axis of the jet, the plasma gas is significantly cooled down in this region as shown in Fig. 4-17. Even a feed rate of copper as small as 5 g min^{-1} leads to a temperature drop of about 2 000 K. Higher feed rates lead to even lower plasma temperatures.

Table 4-4 gives numerical data of the feed rate m_{p} in grams per minute, the mass of copper evaporated, m_{v}, the heat absorbed by the solid particles, Q_{p}, and the heat absorbed by the copper vapor, Q_{v}. Q_{v} is generally much smaller than Q_{p}, and the ratio $Q_{\text{v}}/Q_{\text{p}}$ changes from 29.6% at 1 g min^{-1} feed rate to 4.5% at 20 g min^{-1} feed rate. The total energy absorbed by the powder is between 3.1 and 17.8% of the plasma power input.

4.4.4 Heat Transfer Catastrophy

It is a puzzling but well known fact that the properties of plasma-sprayed coatings vary widely even though the spray parameters have supposedly been fixed within narrow ranges using sophisticated microprocessor-controlled metering devices, and stringent quality control measures have been applied using, for example, SPC and Taguchi analysis. In other words, infinitesimally small changes of the input parame-
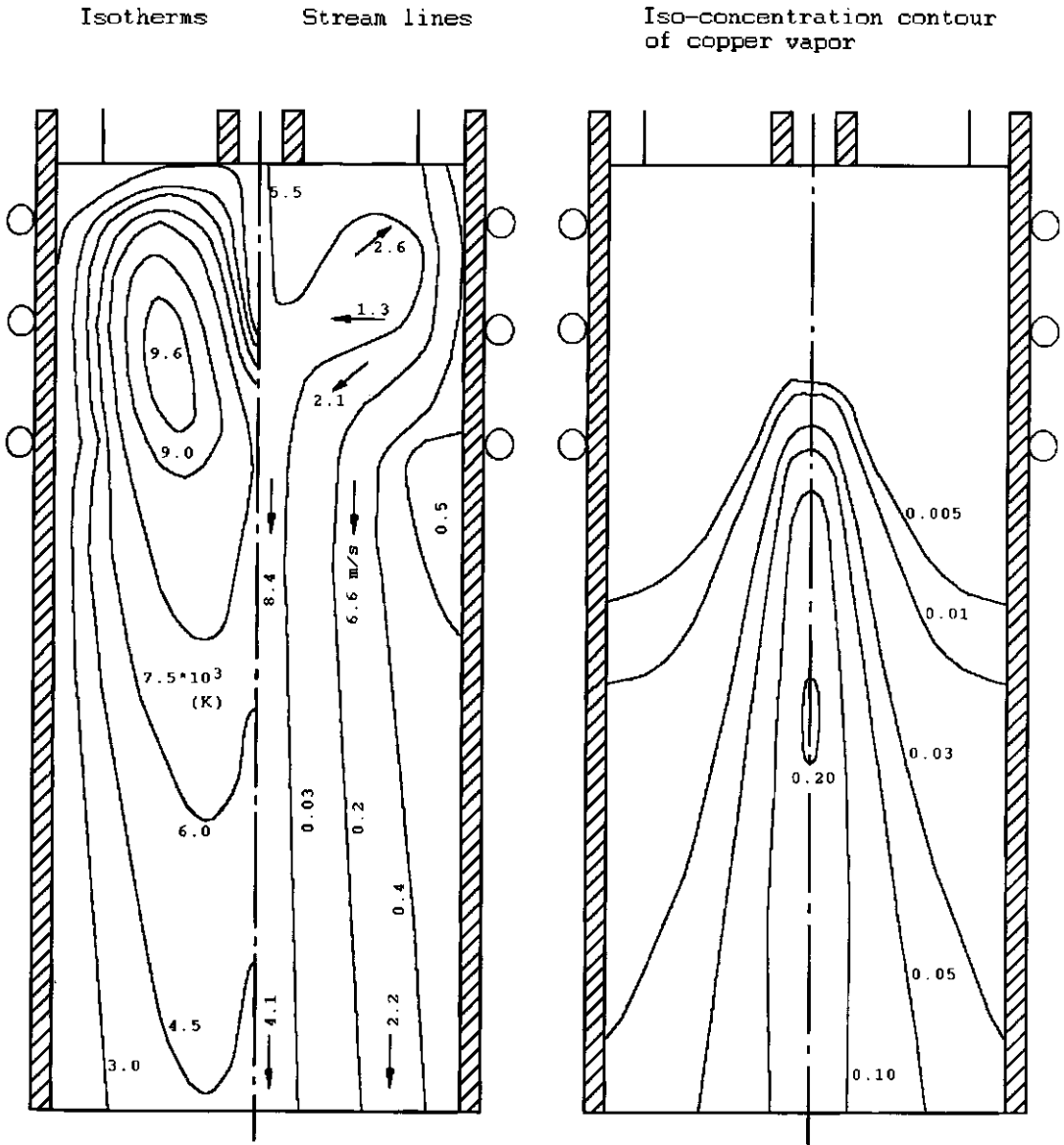
Isotherms   Stream lines   Iso-concentration contour
                                         of copper vapor

Figure 4-16. Cross-section of an inductively-coupled plasmatron after injection of copper powder (5 g min^{-1}). Left: isotherms and stream lines. Right: isopleths of concentration of copper vapor [29].
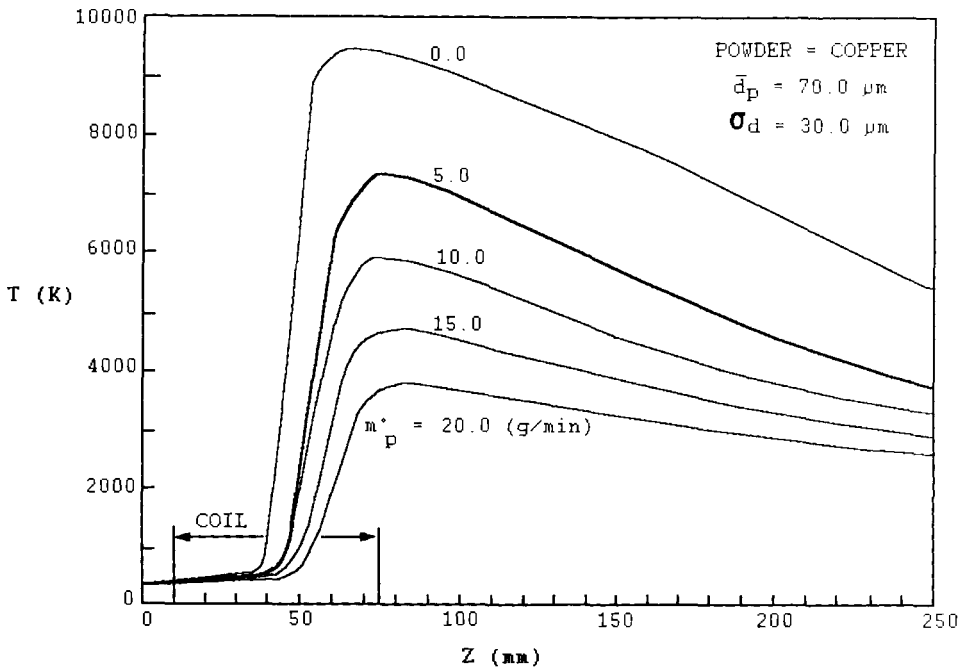
Figure 4-17. Cooling of a plasma under dense loading conditions of copper particles along the centerline of the plasma jet [29].

Table 4-4. Numerical data of plasma power absorbed by copper particles under dense loading conditions [29].

m_p (g min^{-1})	m_v (g min^{-1})	Q_p (W)	Q_v (W)	% of total energy absorbed
1.0	0.50	71.0	21.0	3.1
5.0	1.40	255.0	42.0	9.9
10.0	1.40	386.0	35.0	14.0
15.0	1.16	460.0	28.0	16.3
20.0	0.94	511.0	23.0	17.8

ters cause large, and generally nondeterministic changes in the output parameters, i.e. those parameters influencing the properties and hence the performance of the coatings. This is the hallmark of nonlinearity.

To search for the cause of nonlinear behavior of a collection of particles under dense loading conditions in a plasma jet, several approaches may be taken that all relate to very complex interactions within the plasma. It may suffice to outline in the context of this book only one possible chain of events leading to nonlinearity.

In a thermal plasma cooperative processes occur through numerous types of waves (transverse electromagnetic, longitudinal plasma–acoustic Langmuir, magnetohydrodynamic, and drift waves) that interact and cause stochastic fluctuations

in which the phases of the waves exhibit probabilistic distributions. Such nonequilibrium distributions can be roughly described, respectively as *electromagnetic and magnetohydrodynamic turbulences* (see Sec. 3.1.1). Since both of these turbulences affect the local magnetic field strength, B, and the electrical current density, j, their cross-product, the Lorentz force ($j \times B$) fluctuates rapidly and with it the plasma compression ('z-pinch'). The Lorentz force is being compensated for by the gas kinetic pressure gradient, grad p; consideration of the plasma velocity and viscosity yields the momentum (Navier–Stokes) conservation equation that is known to be nonlinear:

$$(j \times B) = \rho_m u(\text{grad } u) + \text{grad } p - \text{div}(\eta \text{ grad } u), \qquad (4\text{-}49)$$

(see also Eq. (4-46)). Hence changes in the magnitude of the Lorentz force influence the plasma velocity, u, the pressure gradient, grad p, and the dynamic plasma viscosity, η. In particular, the fluctuations of the plasma-confining Lorentz force generate a plasma jet pulsating perpendicular to the jet axis with frequencies that are on the order of the residence time of the particles in the jet, i.e. tenths of microseconds. The rate with which turbulent eddies of cool air surrounding the plasma jet are entrained by the pumping action of the plasma changes accordingly. In this way a rapidly fluctuating temperature profile is obtained with likely rapidly changing heat transfer coefficients, h, of the plasma–particle system. As a consequence the degree of melting of the particles is affected because the relative proportion of heat transferred by convective and radiative processes is severely and instantaneously disturbed. Finally, the local thermal equilibrium breaks down on a scale that is small compared to the overall volume of the plasma jet. Then the system enters the realm of a *'heat transfer catastrophy'*. This phenomenon can be tentatively described in terms of stability theory by an elementary cusp catastrophy of codimension two (Riemann–Hugoniot catastrophy [32]). The order parameters X and Y on the control surface, and the parameter Z separating the control from the behavior surface can be selected in such a way that only dimensionless groups (see Appendix A) as real variables occur (Fig. 4-18). The first ordering parameter X is the heat flux that can be expressed as the product of the Grashof, Prandtl and Nusselt numbers, Gr × Pr × Nu. The second ordering parameter Y is the temperature difference, expressed through the thermal Rayleigh number, Ra. The two ordering parameters define a bifurcation set of local competition between two stable states of heat transfer: a convective heat transfer mode and a radiative heat transfer mode. On the control surface, curves A (radiative mode) and B (convective mode) meet at a temperature-dependent point C with the critical Rayleigh number, Ra_c and a critical heat flux, ξ, beyond which the bimodality ceases to exist. As the parameter defining the z-coordinate the Boltzmann number Bo can be chosen, given by Bo = [Re Pr/St]/ $e^* = $ [Pe/St]/e^*, where Re = Reynolds number, Pr = Prandtl number, Pe = Péclet number, and St = Stefan number, and $e^* = $ surface *emissivity* of the particles.

The behavior surface shows the characteristic shape of the fold of a cusp catastrophy that outlines the region of inaccessibility: heat transfer from plasma to particles occurs either in the convective mode at lower temperature, or in the radiative mode at higher temperature. Consequently, the lower sheet of the behavior surface corresponds to the convective regime B, characterized by a large Boltzmann number
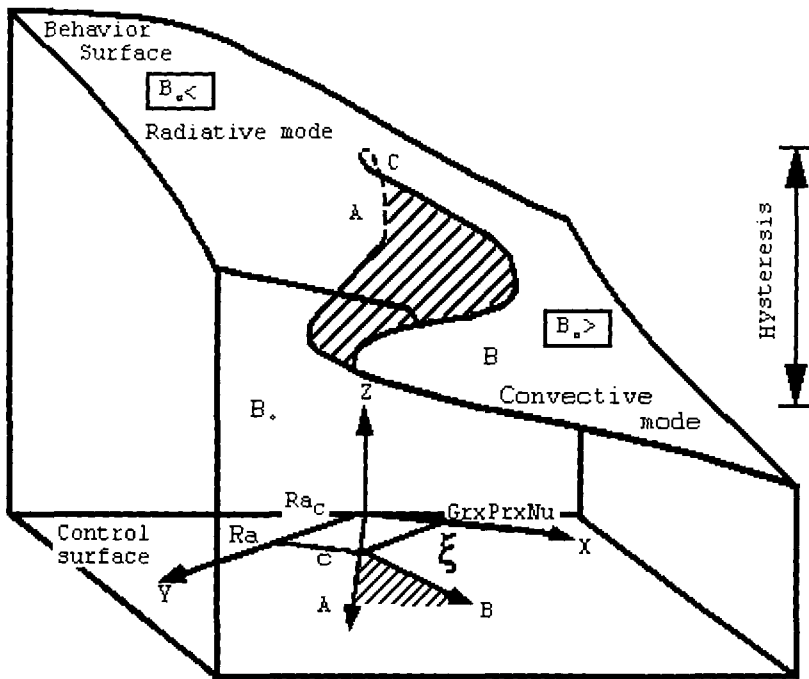
Figure 4-18. Control and behavior surfaces of a plasma undergoing a heat transfer catastrophy (see text).

Bo. The upper sheet corresponds to a radiative regime A with a small Boltzmann number[3]. The Boltzmann number defines the ratio of the bulk heat transport to the heat transported by radiation. For dense loading conditions the Bougue number ($B = 3C_B\lambda_r/4\rho_D r$, with C_B = mass ratio of particles to unit bed volume, λ_r = mean path of radiation, ρ_D = particle density, r = mean particle radius) must be used. This dimensionless group describes the radiant heat transfer to a particle-loaded plasma gas stream. The approach taken here to relate the nonlinear characteristics of a plasma to plasma turbulences with high frequencies and the ensuing heat transfer catastrophy is similar to that of the thermodiffusive mass transport in systems with rapidly changing chemical potential and temperature gradients [33].

4.4.5 Energy Economy

At this point it should be mentioned that only a small fraction of the energy supplied to the plasma gas is being stored in the particles. A macroscopic energy balance [34] shows:

---

[3] The expression for the Boltzmann number is Bo = $\rho_m c_p v_s/e^*\sigma T^3$, with ρ_m = mass density, c_p = specific heat, v_s = plasma velocity, e^* = surface emissivity of the particles, σ = Stefan–Boltzmann coefficient of radiative heat transfer, and T = local plasma temperature.

Table 4-5. Comparison of process variables for welding and plasma spraying operations.

Variable	Unit	CO$_2$ welding	Hand-welding	Plasma-spraying
Deposit mass flow rate	g min^{-1}	42	40	40
Current	A	200	200	400
Voltage	V	25	25	40
Traverse speed	mm s^{-1}	5.5	3.6	40
Weld/spray width	mm	11.5	10	25
Heat content of the spray particles	kJ kg^{-1}	--	--	1 500
Energy efficiency	%	80	80	2.4

Energy supplied to the torch	42.0 kW
Cooling water losses (66%)	−27.7 kW
Losses due to convection and radiation to surroundings	−13.3 kW
Net energy stored in particles	1.0 kW

The energy efficiency is thus only 2.4%. This low number should be compared to a typical energy balance in welding using heat flow density data. Table 4-5 shows process variables for welding and plasma spraying operations. For a *welding process*, the heat flow density is q_w = (efficiency × current × voltage × time)/(traverse speed × weld width × time). For the *plasma spraying process*, it is q_p = (deposit mass flow rate × heat content of particles)/(traverse speed × spray width × time). With the data of Table 4-5 one obtains

$$q_w = (0.8 \times 200[\text{A}] \times 25[\text{V}] \times 1[\text{s}])/(3.6[\text{mm s}^{-1}] \times 10[\text{mm}] \times 1[\text{s}])$$
$$= 111 \text{ J mm}^{-2}$$

$$q_p = (40[\text{g min}^{-1}]/60[\text{s}] \times 1500[\text{J g}^{-1}])/(40[\text{mm s}^{-1}] \times 25[\text{mm}] \times 1[\text{s}])$$
$$= 1 \text{ J mm}^{-2}$$

Consequently, the heat flow density during plasma spraying is only about 1% of that of the standard welding process. In conclusion this means that plasma spraying has a low energy efficiency and a low heat flow density compared with plasma welding.

Similarly low efficiencies have been calculated for plasma-arc wire-spraying operations [35]. Approximately 40% of the input energy is spent to heat the plasmatron and hence is removed by water-cooling whereas the majority of the energy is used to heat the plasma gas. Only 2–5% of this energy is available for melting the wire and accelerating the liquid droplets, and another 6–9% is used to heat the substrate.

The results of the modeling of the momentum and heat transfer could be used on-line for estimating the powder velocities and temperatures at the time of impact. Then a computer-assisted feedback loop could be installed to directly control the input parameters such as:

- power to the plasmatron,
- particle feed rate,
- plasma gas composition, and
- stand-off distance.

To verify the feedback parameters, time-of-flight LDA and multiwavelength pyrometry could be employed. This advanced concept of plasma spray process control, however, is still in the future. Areas of improvement and developments are [36]:

- internal particle heat transfer,
- 3D-models for d.c. plasma spraying,
- verification and control of drag and Nusselt correlations,
- modeling of particle impact on substrate, and
- low pressure, supersonic models for d.c. plasmas.

4.5 Particle Diagnostics: Velocity, Temperature, and Number Densities

The methods of measurement of plasma velocities and plasma temperature, and the equipment used for this purpose have been described in Chapter 3. In this section some typical results related to particle velocities and temperatures, and number densities will be described.

4.5.1 Particle Velocity Determination

As described in detail above, the highly accelerated plasma jet transfers momentum to the powder particles injected near the arc root. The resulting particle velocities have to be chosen in such a way that most particles travel in trajectories that assure optimum residence time in the hot zone of the jet. To obtain axial trajectories an optimum injection velocity is likewise required and thus the powder gas pressure has to be adjusted to the remaining selected plasma parameters. As the flow of the carrier gas controls the particle trajectory through the plasma jet a balance must be maintained between plasma gas and powder carrier gas velocities to correctly position the particles in the plasma for proper melting and acceleration. For a given powder there is an optimum value of powder feed rate that will produce maximum deposition efficiency.

Figure 4-19 shows that for experiments in an argon/hydrogen plasma at a power of 29 kW alumina particles with a mean diameter of $18 \pm 3\,\mu m$ injected with a carrier gas (argon) flow rate of $5.5\,l\,min^{-1}$ move in a trajectory close to and grazing the plasma jet axis. On increasing the powder carrier gas flow rate to $10\,l\,min^{-1}$, the particles completely cross the axis of the jet at a distance of approximately 8 mm from the point of injection [37]. Thus they enter the hotter region of the jet but are blown quickly out of it again so that their residence time in the jet actually decreases.

Figure 4-19. Dependence of the particle trajectories on the flow rate of the argon carrier gas (after [37]).
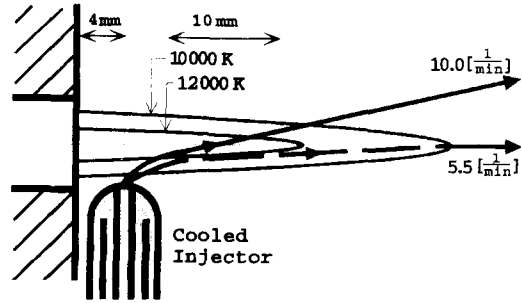

Figure 4-20. Alumina particle velocity profiles at an axial distance of $z = 75$ mm for different argon carrier gas flow rates [37].
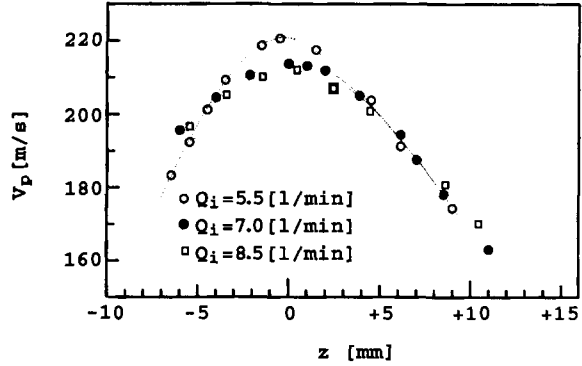

Figure 4-20 shows the particle velocity profiles at an axial distance of $z = 75$ mm for carrier gas flow rates between 5.5 and $8.5 \, \mathrm{l \, min^{-1}}$ [37]. Maximum velocities were obtained with a low carrier gas flow rate ($5.5 \, \mathrm{l \, min^{-1}}$). Under these conditions the majority of the powder particles did occupy trajectories close to the jet axis (see Fig. 4-19) where they acquired the highest momentum and temperature.

It should be noted, however, that the real trajectory of a particle may deviate considerably from the calculated one based on the momentum conservation equation. This has been explained by Vardelle *et al.* [10] by the influence of *thermophoretic forces.* Thermophoresis, however, is strongly dependent on the (free stream) temperature and the particle size [12]. Also, thermophoresis becomes comparable to viscous drag forces only for small relative velocities (around $1 \, \mathrm{m \, s^{-1}}$). Therefore this effect is only significant for very small particles ($<10 \, \mu\mathrm{m}$) that follow very quickly the flow field.

Particle injection can be described in two stages. In the first stage (penetration stage) the particles still maintain the velocities acquired by momentum transfer from the carrier gas. In addition they pick up momentum from the highly accelerated plasma gas. In this stage thermophoretic effects will be negligible since the particle velocities are relatively high even though the temperature gradients are on the order of $10^7 \, \mathrm{K \, m^{-1}}$. But during the following stage of deceleration (relaxation) thermophoretic effects may also be rather insignificant because the temperature gradient decreases rapidly; the displacement of particles will also be small during their short residence time of around 1 ms in the plasma jet [12].
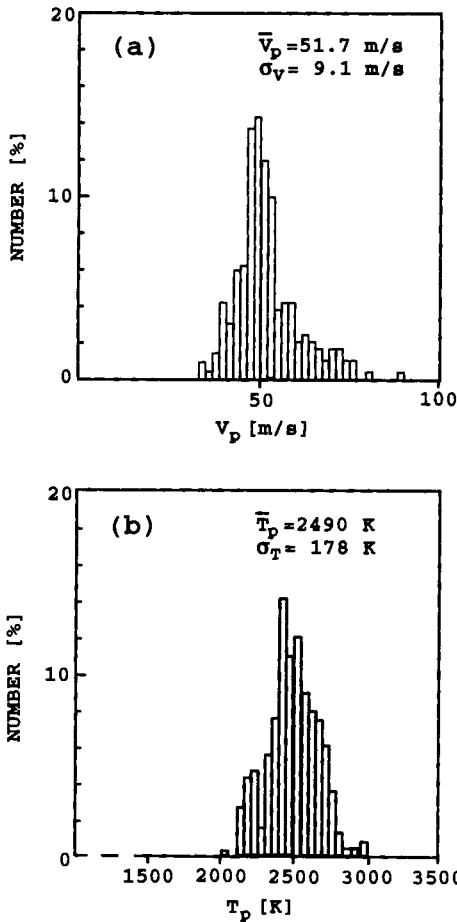
Figure 4-21. Histogram of the velocity (a) and temperature (b) of alumina particles (79 $\pm$ 18 μm diameter) injected with a feed rate of 1.2 g min^{-1} into an inductively-coupled RF argon plasma [38].

The particle velocity distribution assumes frequently a quasi-Gaussian distribution. Figure 4-21a shows a histogram of the velocity of alumina particles of a mean diameter of 79 $\pm$ 18 μm injected with a feed rate of 1.2 g min^{-1} into an inductively coupled RF argon plasma operated under soft-vacuum conditions at a plate power of 15 kW [38]. The powder carrier gas was helium with a flow rate of 8 l min^{-1}. The velocities were measured in-flight simultaneously with particle temperatures (Fig. 4-21b) utilizing the analysis of the change in the time- and amplitude domains of the waveform of a He–Ne laser light pulse. A powder particle with a diameter d_p traverses the observation window of height H and width W. The half-width, t_w, of the laser light pulse corresponds to the time-of-flight of the particle through the slit height. Thus the particle velocity, V_p is:

$$V_p = H/(t_w R),$$ (4-50)

where R = image ratio determined by the optical setup.

Figure 4-22. Dependence of particle velocity on density and grain size of spray powders [40].
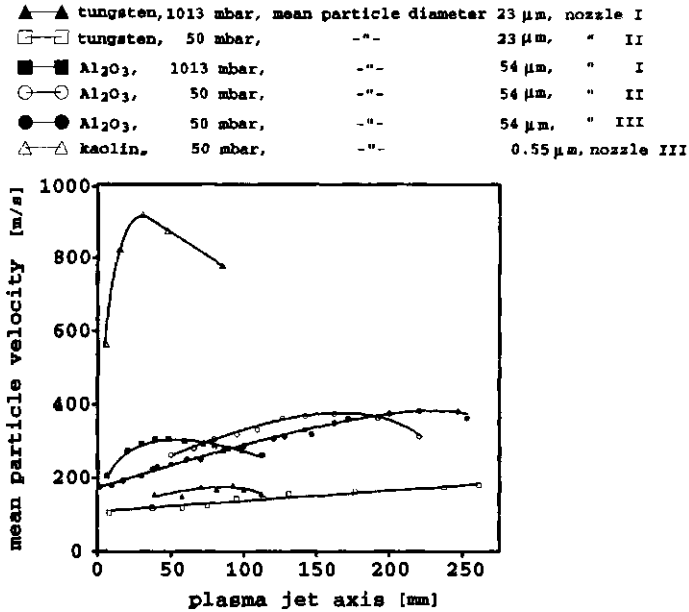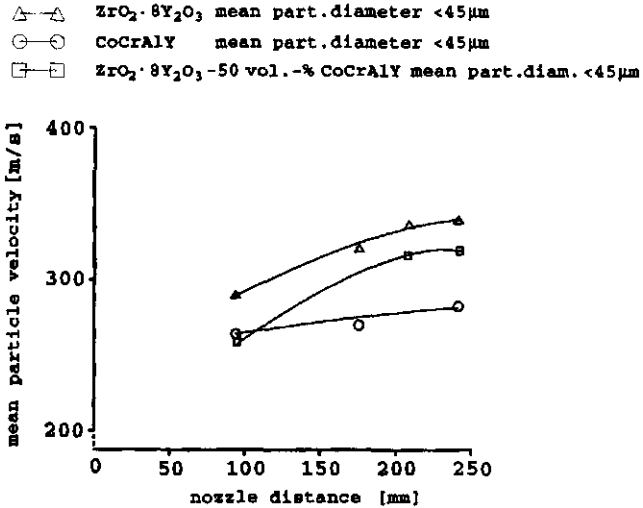
▲——▲	tungsten,1013 mbar,	mean particle diameter 23 µm,	nozzle I
▣——▣	tungsten, 50 mbar,	-"- 23 µm,	" II
■——■	Al₂O₃, 1013 mbar,	-"- 54 µm,	" I
⊖——⊖	Al₂O₃, 50 mbar,	-"- 54 µm,	" II
●——●	Al₂O₃, 50 mbar,	-"- 54 µm,	" III
△——△	kaolin, 50 mbar,	-"- 0.55 µm,	nozzle III

Figure 4-23. Dependence of particle velocity on density of powders utilized in spraying of thermal barrier coatings [40].

△——△	ZrO₂·8Y₂O₃	mean part.diameter <45µm
⊖——⊖	CoCrAlY	mean part.diameter <45µm
▣——▣	ZrO₂·8Y₂O₃-50 vol.-% CoCrAlY mean part.diam.<45µm

The rise time, t_r, and the fall time, t_f, of the trapezoidal profile of the light pulse correspond to the time elapsed between which the particle is entering or leaving the observation window:

$$t_r = t_f = d_p/V_p. \tag{4-51}$$

The pulse intensity, i.e. the amplitude, can give information on the surface temperature of the particle, T_p, as shown in Eq. (3-35).

The particle velocites in the plasma jet are also dependent on the residual chamber pressure. Work by Steffens *et al.* [39] showed that momentum and heat transfer between plasma and particles are reduced at low pressure compared to atmospheric pressure. Modeling of the particle velocity under low pressure ('vacuum') plasma spray conditions require noncontinuum assumptions about the flow conditions [40] (see also [12]). As shown in Figs 4-22 and 4-23 the particle velocities are strongly dependent on density and grain size of the powder materials used. Also, the acceleration of the particles in a low pressure-plasma jet is considerably less than under atmospheric pressure conditions. Figure 4-23, in particular, illustrates the problems associated with the production of graded ceramic/metal coatings as suggested for thermal barrier coatings on gas turbine blades for aerospace applications (see also Sec. 6.2).

4.5.2 Particle Temperature Determination

In principle, the analytical techniques applied to measure in-flight particle temperatures have already been reviewed in the preceding chapter (see Sec. 3.4.1). In order to measure the plasma temperature by two-color pyrometry, very small particles have to be introduced into the plasma jet as seeds that do not disturb the flow of the plasma (Sec. 3.4.1.2).

4.5.3 Particle Number Density Determination

It is of great interest to study simultaneously the velocity, temperature and number density of powder particles in a plasma jet. Any successful modeling requires input
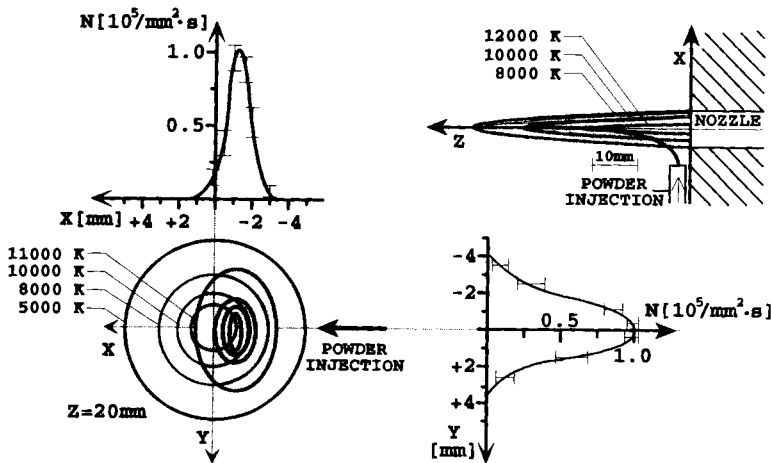

Figure 4-24. Determination of particle flux number densities N in axial and radial directions (alumina, $18 \pm 3\,\mu m$ diameter) [37].
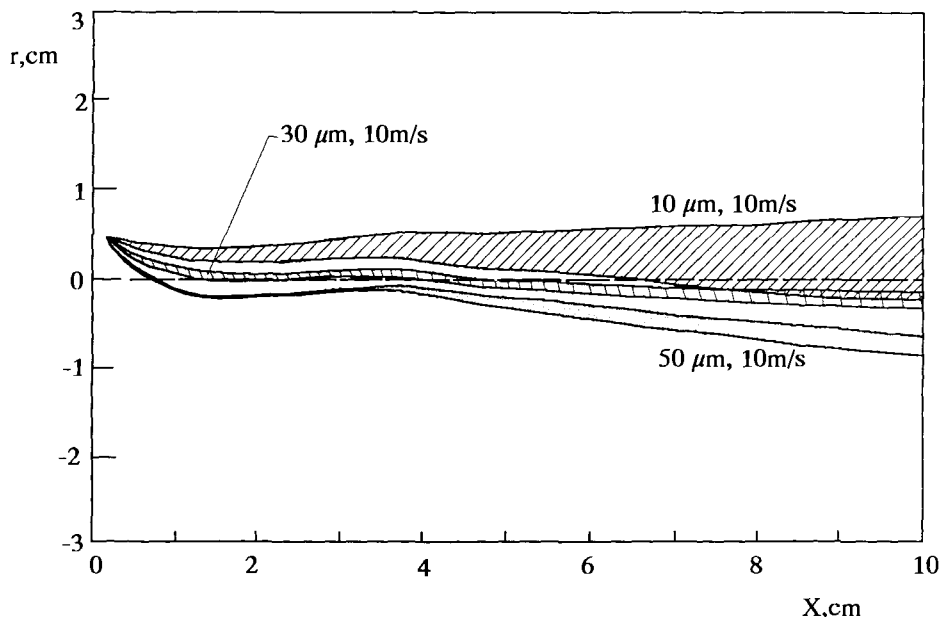
Figure 4-25. Dispersed particle trajectories of alumina particles of different sizes in a turbulent free plasma argon jet [12].

parameters that give reliable information on the numerous forces acting on the powder particles. Equipment has been developed to accomplish the difficult task of measuring simultaneously the three parameters mentioned above (see Fig. 3-31). Typical particle trajectory data and particle flux number density distributions obtained with this equipment are shown in Fig. 4-24. Alumina powder particles (18 $\pm$ 3 μm diameter) were injected with a powder gas flow rate of 5.5 l min^{-1} into an Ar/H$_2$ plasma (29 kW arc power) with a feed rate of 4 g min^{-1}. The tip of the non-cooled powder injection probe was 4 mm from the edge of the nozzle, i.e. 8 mm from the axis of the jet. The particles spread over a large region of the plasma (Fig. 4-24, left, bottom) as shown by the isopleths of the particle flux in the $X-Y$ plane. The profiles of the particle flux number densities are shown in the orthogonal $X-Z$ (top left) and $Y-Z$ (bottom right) planes. There is a noticeable off-center asymmetry in the $X-Z$ plane of injection, indicating the disturbance of the smooth plasma flow by the injected powder. Comparison of these results with those shown in Fig. 4-19 shows that by using a water-cooled injection probe and advancing the point of injection of the powder by only 4 mm towards the plasma jet axis, a substantial modification of the particle trajectories can be observed. As a consequence, in spite of identical carrier gas flow rates in this case the particles penetrate deeper into the jet that results in turn in an acquisition by the particles of larger momentum and higher temperatures.

In the preceding paragraphs the turbulent nature of the plasma jet was not explicitly considered. As the smooth and steady flow field of the plasma is disturbed by

turbulences, the particle trajectories also become dispersed, i.e. the plasma velocity field is locally modified by randomly oriented turbulent eddies [41]. For typical eddy sizes of 1 mm, Fig. 4-25 illustrates the dispersed particle trajectories of alumina particles with mean diameters of 10, 30 and 50 μm injected with a velocity of $10 \, \mathrm{m \, s^{-1}}$ into a turbulent free plasma argon jet [12]. Obviously, smaller particles will be more dispersed than larger ones since the smaller particles are following more easily the turbulent motions within the eddies. Also, the dispersion becomes more prominent when moving downstream from the point of injection due to the accumulated 'random walk' influence. For sufficiently large particles the variable property corrections in the equation of motion (see Eq. (4-1)) may still exceed the turbulent dispersion term. Therefore, a correction for turbulent motion of the plasma can be neglected for larger particles.

References

[1] A. Hasui, S. Kitahara, T. Fukushima, *Trans. NRIM* **1970**, *12*(1), 9.
[2] H. Maruo, Y. Hirata, J. Kato, Y. Matsumoto, *Proc. Intern. Symp. Adv. Thermal Spraying Technol. and Allied Coatings (ATTAC'88)* **1988**, 153.
[3] B. Elvers, S. Hawkins, G. Schulz (eds.), *Ullmann's Encyclopedia of Industrial Chemistry, 5th edition, Metals, Surface Treatment, Vol. A16*, VCH, Weinheim, **1990**, p. 433.
[4] Y. Borisov, N. Voropaj, I. Netesa, V. Korzhyk, I. Kozyakov, *Proc. 14th ITSC'95*, Kobe, 22–26 May, **1995**, 1115.
[5] E. J. Kubel, *Adv. Mater. Proc.* **1990**, *12*, 24.
[6] H. Eschnauer, *Die morphologische Struktur von pulverförmigen Spritzwerkstoffen. Habilitationsschrift*, RWTH Aachen, **1982**.
[7] L. Pawlowski, *The Science and Engineering of Thermal Spray Coatings*, Wiley, Chichester, **1995**, pp. 1–20.
[8] R. B. Heimann, *Development of Plasma-Sprayed Silicon Nitride-Based Coatings on Steel.* Research Report to NSERC and EAITC Canada, 15 December **1992**.
[9] *Powder Technology, Product brochure*, Institute of Materials Science, RWTH Aachen, **1992**.
[10] A. Vardelle, M. Vardelle, P. Fauchais, *Plasma Chem. Plasma Proc.* **1982**, *2*, 255.
[11] J. A. Lewis, W. H. Gauvin, *AIChE J.* **1973**, *19*, 982.
[12] E. Pfender, *Plasma Chem. Plasma Proc.* **1989**, *9*, 167S.
[13] A. V. Nikolaev, In: *Plasma Processing in Metallurgy and in Process Engineering of Non-Organic Materials*, Nauka, Moscow, **1973**.
[14] K. V. Beard, H. R. Pruppacher, *J. Atmos. Sci.* **1969**, *26*, 1066.
[15] J. K. Fiszdon, *Int. J. Heat Mass Trans.* **1979**, *22*, 749.
[16] Y. C. Lee, K. C. Hsu, E. Pfender, *Proc. 5th Int. Symp. on Plasma Chemistry* **1981**, *2*, 795.
[17] X. Chen, E. Pfender, *Plasma Chem. Plasma Phys.* **1983**, *3*, 351.
[18] K. J. Zahnle, *J. Geophys. Res.* **1992**, *97*(10), 243.
[19] N. N. Sayegh, W. H. Gauvin, *AIChE J.* **1979**, *25*, 522.
[20] N. Frösling, *Gött. Beitr. Geophys.* **1938**, *52*, 170.
[21] G. D. Raithby, E. R. Eckert, *Int. J. Heat Mass Trans.* **1968**, *11*, 1233.
[22] M. Vardelle, A. Vardelle, P. Fauchais, M. I. Boulos, *AIChE J.* **1983**, *29*, 236.
[23] X. Chen, E. Pfender, *Plasma Chem. Plasma Phys.* **1983**, *3*, 97.
[24] E. Bourdin, P. Fauchais, M. I. Boulos, *Int. J. Heat Mass Trans.* **1983**, *26*, 567.
[25] D. R. Mash, N. E. Weare, D. L. Walker, *J. Met.* **1961**, *July*, 473.
[26] C. W. Marynowski, F. A. Halden, E. P. Farley, *Electrochem. Technol.* **1965**, *3*, 109.
[27] J. L. Engelke, *Proc. AIChE Meeting*, Los Angles, CA, 5 Feb, **1962**.

[28] X. Chen, E. Pfender, *Plasma Chem. Plasma Proc.* **1982**, *2*, 185.
[29] P. Proulx, J. Mostaghimi, M. I. Boulos, *Int. J. Heat Mass Trans.* **1985**, *28*, 1327.
[30] J. Mostaghimi, P. Proulx, M. I. Boulos, *Int. J. Heat Mass Trans.* **1985**, *28*, 187.
[31] C. T. Crowe, M. P. Sharma, D. E. Stock, *J. Fluid Eng.* **1977**, *99*, 325.
[32] R. Thom, *Structural Stability and Morphogenesis*, Benjamin, New York, NY **1975**.
[33] R. B. Heimann, *Appl. Geochem.* **1987**, *2*, 639.
[34] J. M. Houben, Relations of the Adhesion of Plasma Sprayed Coatings to the Process Parameters Size, Velocity and Heat Content of the Spray Particles. Ph.D. Thesis, Technical University Eindhoven, The Netherlands, **1988**.
[35] N. N. Rykalin, V. V. Kudinov, *Pure Appl. Chem.* **1976**, *48*, 229.
[36] J. Mostaghimi, *Trans. 17th Workshop CUICAC*, (Ed. R. B. Heimann) 1–2 October, **1991**, Quebec, Canada.
[37] M. Vardelle, A. Vardelle, P. Fauchais, M. I. Boulos, *AIChE J.* **1988**, *34*(4), 567.
[38] T. Sakuta, M. I. Boulos, *Proc. 8th Int. Symp. Plasma Chem. ISPC-8*, Tokyo, **1987**, paper BVII-02, p. 371.
[39] H.-D. Steffens, K.-H. Busse, M. Schneider, *Adv. Therm. Spraying*, (Ed. N. F. Eaton) (Proc. 11th ITSC, Montreal, 8–12 Sept.) Pergamon Press, New York, **1986**, *49*.
[40] D. Wei, D. Apelian, M. Paliwal, S. M. Correa, *Proc. Symp. Mat. Res. Soc.* Plasma Processing and Synthesis of Materials, **1984**, *30*, 197.
[41] Y. C. Lee, E. Pfender, *Plasma Chem. Plasma Proc.* **1985**, *5*, 3.